

Title: Altered excitatory and inhibitory neuronal subpopulation parameters are distinctly associated with tau and amyloid in Alzheimer's disease

Kamalini G Ranasinghe^{1*}, Parul Verma², Chang Cai², Xihe Xie², Kiwamu Kudo^{2,3}, Xiao Gao², Hannah Lerner¹, Danielle Mizuiri², Amelia Strom¹, Leonardo Iaccarino¹, Renaud La Joie¹, Bruce L Miller¹, Maria Luisa Gorno-Tempini¹, Katherine P Rankin¹, William J Jagust⁴, Keith Vossel^{1,5}, Gil D Rabinovici^{1,2}, Ashish Raj², Srikantan S Nagarajan²

¹Memory and Aging Center, Department of Neurology, University of California San Francisco, San Francisco, CA 94158

²Department of Radiology and Biomedical Imaging, University of California San Francisco, San Francisco, CA 94143

³Medical Imaging Business Center, Ricoh Company, Ltd., Kanazawa 920-0177, Japan

⁴Helen Wills Neuroscience Institute, UC Berkeley, Berkeley, CA 94720

⁵Mary S. Easton Center for Alzheimer's Disease Research, Department of Neurology, David Geffen School of Medicine, University of California Los Angeles, Los Angeles, CA 90095

*Corresponding author: Kamalini G Ranasinghe, MD PhD
Memory and Aging Center, Department of Neurology
University of California San Francisco
675 Nelson Rising Lane, Suite 190, San Francisco, CA 94158-1207
Tel: 415-514-8847
e-mail: Kamalini.ranasinghe@ucsf.edu

ABSTRACT

Background: Neuronal and circuit level abnormalities of excitation and inhibition are shown to be associated with tau and amyloid-beta (A β) in preclinical models of Alzheimer's disease (AD). These relationships remain poorly understood in patients with AD.

Methods: Using empirical spectra from magnetoencephalography (MEG) and computational modeling (neural mass model; NMM) we examined excitatory and inhibitory parameters of neuronal subpopulations and investigated their specific associations to regional tau and A β , measured by positron emission tomography (PET), in patients with AD.

Results: Patients with AD showed abnormal excitatory and inhibitory time-constants and neural gains compared to age-matched controls. Increased excitatory time-constants distinctly correlated with higher tau depositions while increased inhibitory time-constants distinctly correlated with higher A β depositions.

Conclusions: Our results provide critical insights about potential mechanistic links between abnormal neural oscillations and cellular correlates of impaired excitatory and inhibitory synaptic functions associated with tau and A β in patients with AD.

Funding: This study was supported by the National Institutes of Health grants: K08AG058749 (KGR), F32AG050434-01A1 (KGR), K23 AG038357 (KAV), P50 AG023501, P01 AG19724 (BLM), P50-AG023501 (BLM & GDR), R01 AG045611 (GDR); AG034570, AG062542 (WJ); NS100440 (SSN), DC176960 (SSN), DC017091 (SSN), AG062196 (SSN); a grant from John Douglas French Alzheimer's Foundation (KAV); grants from Larry L. Hillblom Foundation: 2015-A-034-FEL and (KGR); 2019-A-013-SUP (KGR); a grant from the Alzheimer's Association: (PCTR-B-13-288476) (KAV), and made possible by Part the CloudTM, (ETAC-09-133596); a grant from Tau Consortium (GDR & WJJ), and a gift from the S. D. Bechtel Jr. Foundation.

Key-words: Alzheimer's disease; Network hyperexcitability; Excitatory-Inhibitory imbalance; Magnetoencephalography; A β -PET, Tau-PET, Neural mass model; Spectral power; Neural oscillations.

1. INTRODUCTION

Aggregation and accumulation of amyloid beta (A β) and tau proteins is a defining feature of Alzheimer's disease (AD) pathophysiology([Braak and Braak, 1991](#)). Although the mechanisms by which AD proteinopathy exerts its effects remain an area of active research, disruption of the fine balance between excitatory and inhibitory neuronal activity has emerged as a potential driver for network dysfunction contributing to cognitive deficits in AD ([Palop et al., 2006](#); [Harris et al., 2020](#)). Preclinical AD models have demonstrated direct effects of tau and A β leading to impaired function in excitatory pyramidal neurons as well as inhibitory interneurons ([Palop et al., 2007](#); [Hoover et al., 2010](#); [Sun et al., 2012](#); [Verret et al., 2012](#); [Palop and Mucke, 2016](#); [Zhou et al., 2017](#); [Busche et al., 2019](#); [Zott et al., 2019](#); [Harris et al., 2020](#); [Chang et al., 2021](#)). In patients with AD, abnormalities in brain oscillations([Ranasinghe et al., 2014](#); [Nakamura et al., 2018](#); [Maestu et al., 2019](#); [Babiloni et al., 2020](#); [Ranasinghe et al., 2020](#)), which are essentially determined by relative contributions of excitatory and inhibitory synaptic currents([Buzsaki et al., 2012](#)), are a display of perturbed balance of excitation and inhibition in local circuits. However, despite the fact that clinical studies have demonstrated associations between abnormal oscillatory signatures and AD proteinopathy([Nakamura et al., 2018](#); [Smailovic et al., 2018](#); [Pusil et al., 2019](#); [Ranasinghe et al., 2020](#); [Ranasinghe et al., 2021](#)), the electrophysiological basis of aberrant excitatory and inhibitory activity of neuronal cell populations and how these relate to A β and tau in patients with AD remain largely unknown.

The goal of this study was to identify impaired neuronal parameters in excitatory and inhibitory neuronal subpopulations and determine their specific associations to regional A β and tau pathology in AD patients. We combined spectral signatures derived from magnetic field potentials via non-invasive imaging in AD patients with mathematical modeling (neural mass model; NMM)([David and Friston, 2003](#); [Raj et al., 2020](#); [Verma et al., 2022](#)), to estimate excitatory and inhibitory neuronal parameters. Specifically, we hypothesized that abnormal regional spectral signatures in AD patients related to altered activity of excitatory and inhibitory neuronal subpopulations will be distinctly associated with tau and A β depositions. We combined NMM, and multimodal imaging data from: magnetoencephalography (MEG), A β -, and tau-positron emission tomography (PET), in a well

characterized cohort of AD patients. First, we leveraged the millisecond temporal resolution and superior spatial resolution of MEG signal to derive the oscillatory signatures of local neuronal synchrony. Next, we used a linearized NMM, which was recently described as a component of a spectral graph model, and which successfully reproduced the empirical macroscopic properties of oscillatory signatures([Raj et al., 2020](#);[Verma et al., 2022](#)), to derive excitatory and inhibitory parameters of local neuronal ensembles. We then examined the specific associations of altered excitatory and inhibitory neuronal subpopulation parameters and A β - and tau-tracer uptake patterns and how these contribute to produce the characteristic spectral changes in AD patients.

2. METHODS

2.1. Participants

Twenty patients with AD (diagnostic criteria for probable AD or MCI due to AD)([Albert et al., 2011](#);[McKhann et al., 2011](#);[Jack et al., 2018](#)) and 35 age-matched controls were included in this study (Table 1). Each participant underwent a complete clinical history, physical examination, neuropsychological evaluation, brain magnetic resonance imaging (MRI), and a 10-minute session of resting MEG. All AD patients underwent PET with Tau-specific radiotracer, ^{18}F -flortaucipir and A β -specific radiotracer, ^{11}C -PIB. Twelve AD patients in this study cohort overlapped with our previous multimodal imaging investigation of long-range synchrony assay([Ranasinghe et al., 2020](#)). All participants were recruited from research cohorts at the University of California San Francisco (UCSF) ADRC. Informed consent was obtained from all participants and the study was approved by the Institutional Review Board (IRB) at UCSF.

2.2. Clinical assessments and MEG, PET and MRI acquisition and analyses

AD patients were assessed via MMSE and a standard battery of neuropsychological tests. All participants were assessed via a structured caregiver-interview to determine the Clinical Dementia Rating (CDR) (Appendix methods).

MEG scans were acquired on a whole-head biomagnetometer system (275 axial gradiometers; MISL, Coquitlam, British Columbia, Canada) for 5-10 minutes, following the same protocols described previously([Ranasinghe et al., 2020](#)). Tomographic reconstructions of source space data was done using a continuous 60s data epoch, an individualized head model based on structural MRI, and a frequency optimized adaptive spatial filtering technique implemented in the Neurodynamic Utility Toolbox for MEG (NUTMEG; <http://nutmeg.berkeley.edu>). We derived the regional power spectra for frequency bands: 2-7Hz delta-theta, 8-12Hz alpha, 13-35Hz beta, and 1-35Hz broad-band, from FFT and then converted to dB scale (Appendix methods).

Flortaucipir and PiB-PET acquisitions were done based on the same protocols detailed previously([Scholl et al., 2016](#)). Standardized uptake value ratios (SUVR) were created using Freesurfer-defined cerebellar gray matter for PIB-PET. For ¹⁸F-flortaucipir, Freesurfer segmentation was combined with the SUIT template to include inferior cerebellum voxels avoiding contamination from off target binding in the dorsal cerebellum (Appendix methods).

2.3. Mathematical modeling and parameter estimation

We used a linearized neural mass model (NMM)([Raj et al., 2020](#);[Verma et al., 2022](#)) to estimate excitatory and inhibitory neuronal subpopulation parameters. In this regional-model, for every region k , (k varies from 1 to N and N is the total number of regions) based on the Desikan-Killiany parcellation the regional population signal is modeled as the sum of excitatory signals $x_e(t)$ and inhibitory signals $x_i(t)$. Both excitatory and inhibitory signal dynamics consist of a decay of the individual signals with a fixed neural gain, incoming signals from populations that alternate between the excitatory and inhibitory signals, and input Gaussian white noise. The equations for the excitatory and inhibitory signals for every region are the following:

$$\frac{dx_e(t)}{dt} = -\frac{f_e(t)}{\tau_e} * (g_{ee}x_e(t) - g_{eif_i}(t) * x_i(t)) + p(t)$$

$$\frac{dx_i(t)}{dt} = -\frac{f_i(t)}{\tau_i} * (g_{ii}x_i(t) + g_{eif_e}(t) * x_e(t)) + p(t)$$

where \star stands for convolution; parameters g_{ee} , g_{ii} , and g_{ei} are neural gains for the excitatory, inhibitory, and alternating populations, respectively; τ_e and τ_i are time-constants of excitatory and inhibitory populations, respectively; $p(t)$ is the input Gaussian white noise; $f_e(t)$ and $f_i(t)$ are Gamma-shaped ensemble average neural impulse response functions (Appendix methods for step-by-step details). The parameters, g_{ee} , g_{ii} , τ_e , and τ_i were estimated for each region-of-interest (ROI) and parameter g_{ei} was fixed at 1. Each region's spectra were modeled using the above equations, and the power spectral density was generated for frequencies 1-35 Hz. The goodness of fit of the model was estimated by calculating the Pearson's correlation coefficient between the simulated model power spectra and the empirical source localized MEG spectra for frequencies 1-35 Hz. This goodness of fit value was used to estimate the model parameters. Parameter optimization was done using the basin hopping global optimization algorithm in Python ([Wales and Doye, 1997](#)). The model parameter values and bounds were specified as: 17 ms, 5ms, and 30 ms, respectively, for initial, upper-boundary and lower-boundary, for τ_e , and τ_i ; 0.5, 0.1 and 10, respectively, for initial, upper-boundary and lower-boundary, for g_{ee} and g_{ii} . The hyperparameters of the algorithm which included the number of iterations, temperature, and step-size were set at 2000, 0.1, and 4, respectively. If any of the parameters was hitting the specified bounds, parameter optimization was repeated with a step-size of 6 for that specific ROI, and finally the set of parameters which led to a higher Pearson's correlation coefficient was chosen. The cost function for this optimization was negative of Pearson's correlation coefficient between the source localized MEG spectra in dB scale and the model power spectral density in dB scale as well. This procedure was performed for every ROI of every subject.

2.4. Statistical analyses

Statistical tests were performed using SAS® software (SAS9.4; SAS Institute, Cary, NC). To compare the demographics and clinical characteristics between controls and patients with AD we used unpaired t-tests for age, Pearson χ^2 test for sex and handedness, Fisher's exact test for race, Wilcoxon-Mann-Whitney test for education, MMSE, CDR and CDR-SOB.

We used a one-way ANOVA to compare the broad-band power spectra between controls and patients, and a two-way-ANOVA model to compare across the three frequency bands, delta-

theta, alpha and beta. Each model included a repeated measures design to incorporate the 68 cortical ROIs per subject. Post-hoc comparisons were derived from comparing least-squares means with the adjustment of multiple comparisons using Tukey-Kramer test. The regional patterns of spectral power distributions incorporated unpaired t-tests at regional level and thresholded with 10% false discovery rate.

To compare the neuronal parameters between the controls and patients we used a linear mixed effects model (PROC MIXED) with repeated measures design to incorporate the multiple ROIs per subject. We reported the estimated least-squares means and the statistical differences of least-squares means based on unpaired t-tests.

We ran mixed effect models to examine the associations between tau- and A β -trace uptake and excitatory and inhibitory neuronal parameters derived from NMM. The predictor variables of models included the flortaucipir (tau) SUVR and ^{11}C -PIB (A β) SUVR, at each ROI in patients with AD. We ran separate mixed effect models including the dependent variable of z-score measures depicting the change of each neuronal parameter in patients, based on age-matched control cohort, including the neuronal time-constants, τ_e and τ_i , and neural gains, g_{ee} and g_{ii} . Each model included a repeated measures design to incorporate the 68 ROIs per subject and modeled the heterogeneity in residual variances at ROI. Mixed models to examine the associations between average scaling difference between the MEG spectra and the model output did not show any significant relationships.

We ran separate mixed effect models where the dependent variable included the z-score measures depicting the change of spectral power in patients, based on age-matched control cohort, within (1) broad-band spectrum (1-35 Hz); (2) delta-theta spectrum (2-7 Hz); (3) alpha spectrum (8-12 Hz) (4) beta spectrum (13-35 Hz). Each model included a repeated measures design and modeled the heterogeneity in residual variances at ROI.

We utilized the PROC MIXED procedure in SAS to perform mediation analysis ([Bauer et al., 2006](#)) to test the hypothesis that distinct effects of tau and A β on the frequency-specific spectral power changes would be mediated via their unique modulatory effects on τ_e and τ_i , respectively.

Specifically, we examined: (1) the direct and τ_i mediated effects of A β on delta-theta power; (2) the direct and τ_e mediated effects of tau on alpha power; and (3) the direct and τ_e mediated effects of tau on beta power.

3. RESULTS

On average, the patients were mild to moderately impaired with a mean Mini Mental state Exam score of 22.8 ± 4.5 (MMSE range: 22–26), mean Clinical Dementia Rating of 0.72 ± 0.47 (CDR range: 0.5–0.8), and mean CDR-Sum of Boxes of 3.8 ± 2.5 , with characteristic cognitive deficits (Table 1; Appendix table 1).

Table 1. Participant demographics and clinical characteristics.

Characteristic	Controls (N=35)	Patients with AD (N=20)	P *
Age – yr	$69.3.6 \pm 8.4$	66.3 ± 9.8	0.237
Female sex – no. (%)	20 (57.1)	11 (55.0)	0.876
White – no. (%) [†]	30 (90.9)	20 (100.0)	0.282
Education – yr	18 (16 – 18)	18 (16 – 18)	0.855
Right handedness – no. (%)	30 (85.7)	17 (85.0)	0.340
MMSE [‡]	30 (29 – 30)	23 (22 – 26)	<.0001
CDR [§]	0 (0 – 0)	0.5 (0.5 – 0.8)	<.0001
CDR-SOB [§]	0 (0 – 0)	3.5 (2.3 – 4.3)	<.0001
Age at disease onset	.	59.4 ± 9.39	.
Disease duration	.	6.9 ± 2.4	.

Values for age, age at disease onset and disease duration are means \pm SD. Values for education, Mini Mental State Exam (MMSE), Clinical Dementia Rating (CDR) and CDR-Sum of Boxes (CDR-SOB), are medians with interquartile ranges within parentheses. *Statistical tests: P values are reported from unpaired t-test for age, Pearson χ^2 test for sex and handedness, Fisher's exact test for race, Wilcoxon-Mann-Whitney test for education, MMSE, CDR and CDR-SOB. [†]Race or ethnic group was self-reported. Two control participants opted out from reporting the race. [‡]Scores on the MMSE range from 0 to 30, with higher scores denoting better cognitive function. [§]Scores on the CDR range from 0 to 3 and scores on the CDR-SOB range from 0 to 18, with higher scores denoting more disability. AD = Alzheimer's disease.

3.1. Regional spectral changes in AD: increased delta-theta and reduced alpha and beta

Patients with AD showed a clear leftward shift in their power spectra when compared to age-matched controls. Specifically, AD patients showed a reduced spectral power within alpha (CI,

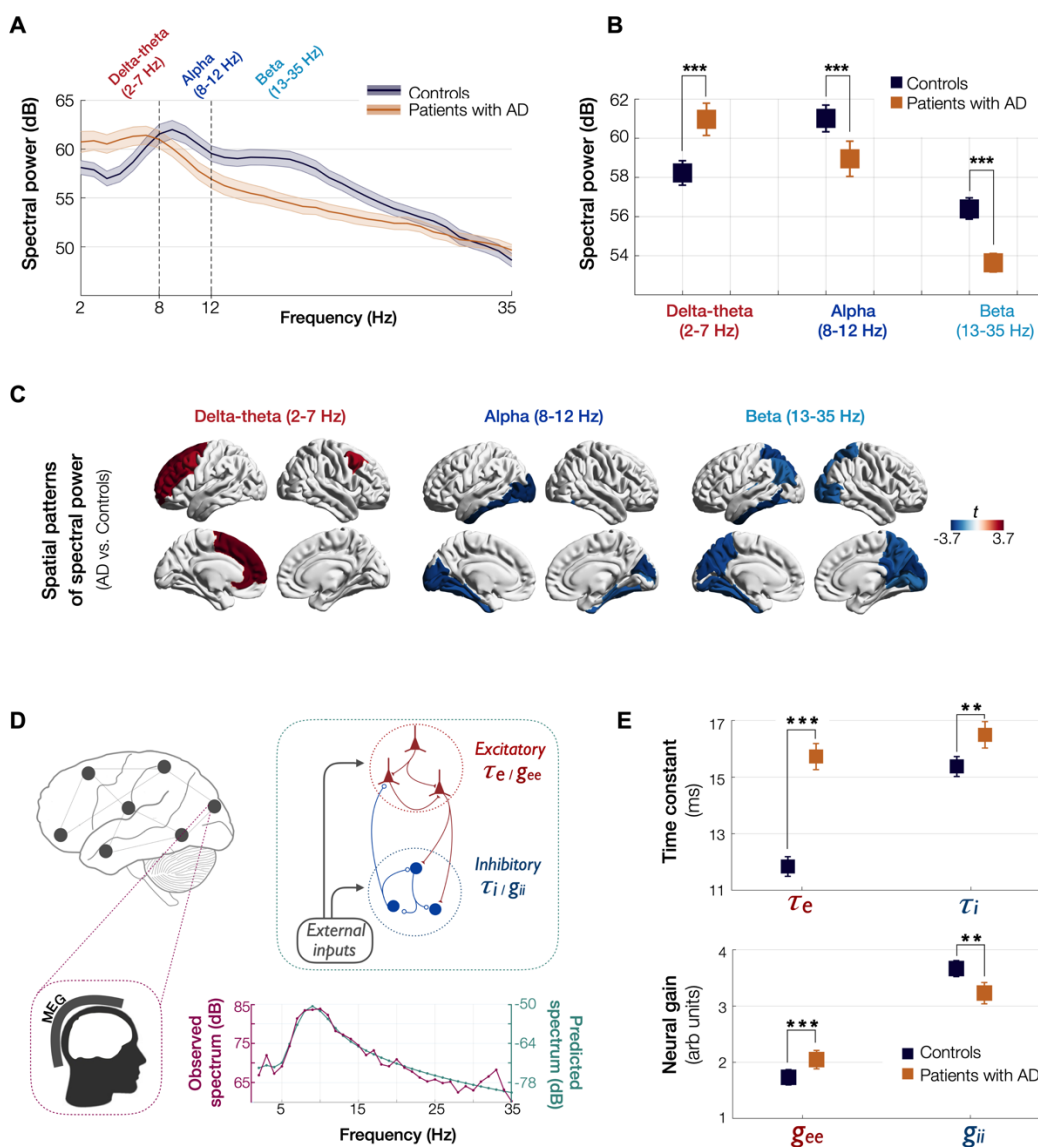


Figure 1 Spectral power changes and altered excitatory and inhibitory neuronal subpopulations parameters in patients with AD.

Patients with AD showed higher delta-theta (2-7 Hz) spectral power and lacked a clear alpha peak (8-12 Hz) as opposed to controls (A). A two-way-ANOVA comparing patients and controls showed significantly higher spectral power within delta-theta frequency band and showed significantly lower spectral power within alpha and beta (13-35 Hz) bands, in patients with AD (B). The markers depict the least-square means, and the error-bars depict the 95% confidence intervals. Regional patterns of spectral power changes in patients with AD showed increased delta-theta power is predominant in the frontal regions and reduced alpha and beta spectral power is predominant in the temporoparietal and occipital cortices (C). Images show the *t*-values from statistical comparison of regional data based on DK atlas parcellations and thresholded at FDR 10%. Schematic representation of the linear neural mass model (NMM) and an example model prediction (D). Linear NMM represents the local assemblies of excitatory and inhibitory neurons into lumped linear systems, at each region-of-interest (ROI). External inputs and outputs are gated through both excitatory and inhibitory neurons. The recurrent architecture of the two pools within a local area is captured by the neuronal time-constants, τ_e and τ_i , and neural gain terms, g_{ee} and g_{ii} , indicating the loops created by recurrences within excitatory, inhibitory and cross-populations. At each ROI, the model delivers these parameters as it predicts the broad-band spectrum (1-35 Hz) optimized to the empirical spectrum derived from MEG. Patients with AD showed significantly increased neuronal time-constants, τ_e and τ_i compared to age-matched controls (E). Patients with AD also showed increased excitatory neural gain (g_{ee}) and reduced inhibitory neural gain (g_{ii}) than controls (c). The markers and error-bars depict the least-square means and 95% confidence intervals. Abbreviations: AD, Alzheimer's disease; MEG, magnetoencephalography.

58.04-59.85dB, 60.33-61.69dB, AD and controls, respectively) and beta (CI, 53.16-54.11B, 56.03-56.75dB, AD and controls, respectively) but increased power within delta-theta bands (60.14-61.79dB, 57.60-58.85dB, AD and controls, respectively) (Figure.1A-B). A direct region-wise comparison showed a frontal predominant spatial distribution for the spectral power increase within delta-theta and a posterior predominant distribution for the spectral power reduction in alpha and beta (Figure.1C). These results demonstrate the frequency specific and region dependent characteristics of oscillatory abnormalities in AD patients.

3.2. Estimated neural mass model parameters demonstrate altered excitatory and inhibitory subpopulation activity

We used a linear NMM, capable of reproducing spectral properties of neural activity, to predict the empirical spectra at regional level (i.e., 68 cortical regions) in patients with AD and controls. NMM predicted four parameters for neuronal populations: the excitatory time-constant (τ_e), inhibitory time-constant (τ_i), excitatory neural gain (g_{ee}), and inhibitory neural gain (g_{ii}). Specifically, in each subject, and for each cortical region, the NMM parameters were estimated for the best fit (highest Pearson correlation coefficient) between observed MEG power spectrum and the NMM spectrum (Figure.1D; Appendix figure.1). Statistical mixed models with repeated measures demonstrated that AD patients have significantly increased time-constant parameters of excitatory and inhibitory neurons (τ_e and τ_i) than controls (Figure.1E; τ_e : CI, 15.27-16.19, 11.49- 2.18; $P<0.0001$; τ_i : CI, 16.03-16.96, 15.02-15.73; $P=0.0002$, AD and controls, respectively; Appendix figure.2A-B). Furthermore, AD patients showed increased g_{ee} and reduced g_{ii} compared to controls indicating abnormal neural gains in both excitatory and inhibitory subpopulations (Figure.1E; g_{ee} : CI, 1.88-2.21, 1.59-1.87; $P=0.0005$; g_{ii} : CI, 3.04-3.42, 3.52-3.81; $P=0.0003$, AD and controls, respectively; Appendix figure.2C-D).

3.3. Tau and A β distinctly modulate excitatory and inhibitory time-constants, respectively.

Next, we examined the functional associations of model parameters with flortaucipir (tau) and ^{11}C -PiB (A β) uptake patterns (Appendix figure.2E-F). linear mixed effects models showed that increased τ_e was correlated with higher tau-tracer uptake, while increased τ_i was correlated with higher A β -

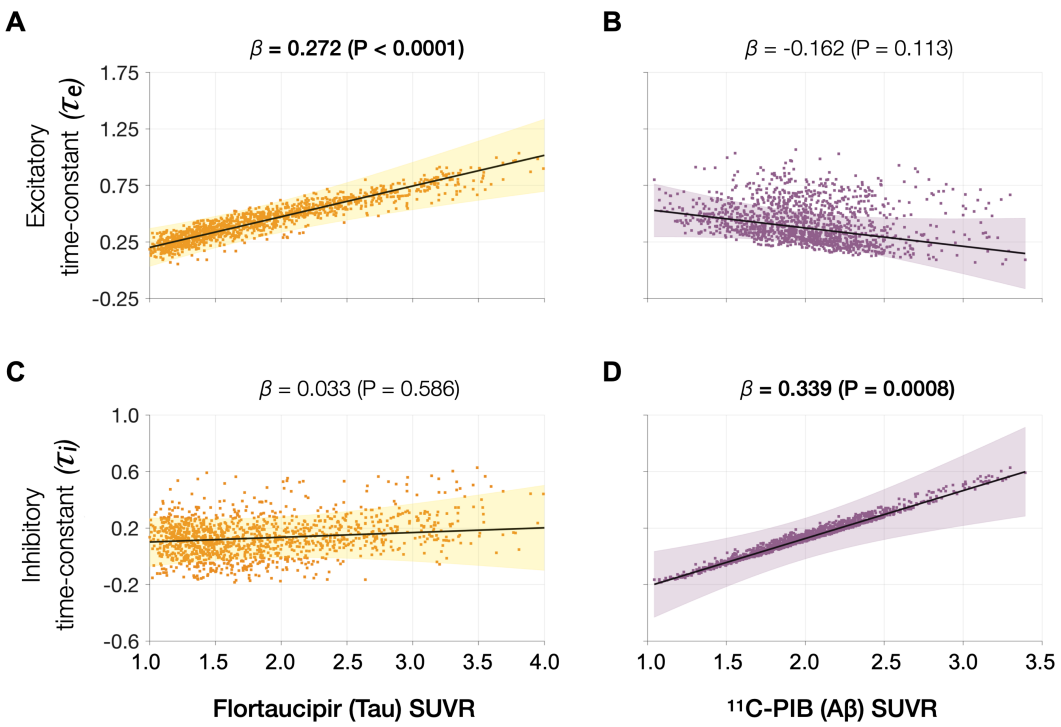


Figure. 2 Associations between tau- and A β -tracer uptake and excitatory and inhibitory neuronal time-constants in patients with AD.

Increased time-constants showed distinct associations with tau and A β in AD patients. Increased excitatory time-constant (τ_e) was positively correlated with tau, but not with A β (A, B). Increased inhibitory time-constant (τ_i) was positively correlated with A β , but not with tau (C, D). Subplots A-D indicate the model estimates from linear mixed effects models predicting the changes (z-scores) in each neuronal parameter from flortaucipir (tau) SUVR and ^{11}C -PiB (A β) SUVR, in patients with AD. The fits depicting tau predictions were computed at the average SUVR of A β (1.99), and the fits depicting A β were computed at average SUVR of tau (1.64). The scatter plots indicate the predicted values from each model incorporating a repeated measures design. Abbreviations: AD, Alzheimer's disease; A β , amyloid-beta.

tracer uptake (Figure.2A&D; τ_e :tau, $t=4.11$, $P<0.0001$; τ_i : A β , $t=3.38$, $P=0.0008$). In contrast, there were no correlations between τ_e and A β -tracer uptake and between τ_i and tau-tracer uptake (Fig.2B&C; τ_e : A β , $t=-1.59$, $P=0.1131$; τ_i : tau, $t=0.54$, $P=0.5863$). In contrast to time-constant associations, altered neural gains did not show statistically significant associations to either flortaucipir or ^{11}C -PiB uptakes (Appendix figure.3). Distinctive association of tau with excitatory time-constants and A β with inhibitory time-constants may support the hypothesis of distinct roles of tau and A β mediated pathomechanisms on excitatory and inhibitory synaptic functions.

3.4. Spectral changes associated with tau and A β are partially mediated by altered excitatory and inhibitory time-constants.

Next, we tested the hypothesis that effects of tau and A β on the frequency-specific spectral power changes would be mediated by their unique modulatory effects on τ_e and τ_i , respectively. To this

end, we first demonstrated the specific relationships between frequency-specific spectral changes and regional tracer uptake (flortaucipir and ^{11}C -PiB). Consistent with previous reports (Canuet et al., 2015; Nakamura et al., 2018; Pusil et al., 2019; Ranasinghe et al., 2020), linear mixed model analyses showed that associations of tau and A β on the power spectrum were frequency specific. For example, delta-theta was only associated with A β (positive correlation) and showed no associations to tau (Figure 3A-B). In contrast, alpha and beta power spectra showed significant associations to both tau and A β , where higher tau reduced spectral power and higher A β

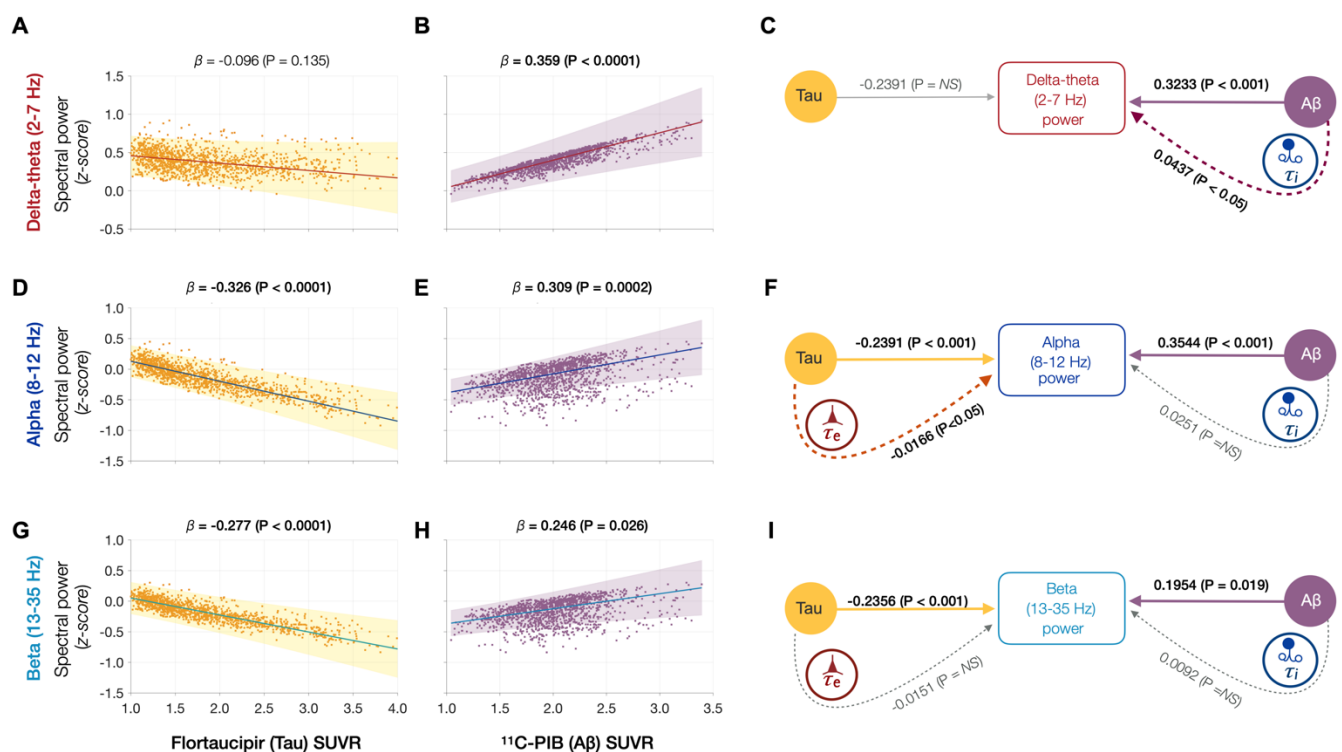


Figure 3 Frequency-specific spectral power modulations of tau and A β are partially mediated via increased excitatory (τ_e) and inhibitory (τ_i) time-constants.

Associations between tau- and A β -tracer uptake and spectral power changes in patients with AD are depicted in subplots A, B, D, E, G, H. Tau was not associated with the delta-theta (2-7 Hz) spectral changes (A), while it was positively modulated by A β (B). Both alpha (8-12 Hz), and beta (13-35 Hz) spectra showed significant negative associations with tau (D, G) and significant positive associations with A β (E, H). Subplots indicate the model estimates from linear mixed effects analyses predicting the spectral power changes from flortaucipir (tau) SUVR and ^{11}C -PiB (A β) SUVR, for patients with AD. The fits depicting tau predictions were computed at the average SUVR of A β (1.99), while the fits depicting A β were computed at average SUVR of tau (1.64). The scatter plots indicate the predicted values from each model incorporating a repeated measures design to account for 68 regions per subject. Subplots C, F and I depicts mediation models to examine the direct effects of tau and A β , and the effects mediated through excitatory (τ_e) and inhibitory (τ_i) time-constants on different frequency bands. Delta-theta power increases were significantly affected by A β and was partially mediated through the effect of A β on inhibitory (τ_i) time-constant (C). Alpha power reductions were affected by tau and a small, but a significant fraction of this effect was mediated through the effect of tau on excitatory (τ_e) time-constant (F). Beta power reductions were significantly affected by tau, although there was no statistically significant effect mediated through the effect of tau on excitatory (τ_e) time-constant (I). A β effects on alpha and beta spectral changes were only direct effects with no statistically significant effects mediated through altered inhibitory (τ_i) time-constants. Abbreviations: AD, Alzheimer's disease; A β , amyloid-beta; SUVR, standardized uptake value ratio.

increased spectral power (Figure.3D-E and G-H). Including regional cortical atrophy as a covariate into models did not influence these relationships indicating that spectral changes are robust to neuronal loss (Appendix figure.4). In summary, delta-theta power was uniquely associated with A β while reduced alpha and beta spectral power was the result of a dual modulation by tau and A β with a net negative modulatory effect from tau.

Next, we used a mediation analysis to examine whether the distinct effects of tau and A β on frequency-specific spectral changes are mediated via τ_e and τ_i , respectively. The mediation analyses specifically examined: (1) the direct and τ_i mediated effects of A β on delta-theta power; (2) the direct and τ_e mediated effects of tau on alpha and beta power; and (3) the direct and τ_i mediated effects of A β on alpha and beta power. We found that A β modulation of delta-theta power was significantly mediated through τ_i in addition to direct modulation (Figure.3C). We also found that tau modulation of alpha power was significantly mediated through τ_e in addition to the direct modulation (Figure.3F), whereas A β modulation of alpha power was only through a direct effect. Tau as well as A β modulation of beta power occurred only through direct effects (Figure.3I). Collectively, τ_e and τ_i partially mediated the effects of AD proteinopathy towards the signature spectral change observed in AD.

4. DISCUSSION

This is the first study, in patients with AD, showing quantitative links between altered neuronal subpopulation dynamics of excitatory and inhibitory function with abnormal accumulations of tau and A β . We combined electrophysiology, molecular imaging, and NMM model, to examine the excitatory and inhibitory parameters of regional neural subpopulations in patients with AD and how these relate to tau and A β depositions. AD patients showed abnormal excitatory and inhibitory neuronal parameters compared to controls and with distinct associations to tau and A β where higher tau correlated with increased excitatory time-constants and higher A β correlated with increased inhibitory time-constants. Furthermore, the frequency specific associations of spectral changes to tau and A β were partially mediated by increased excitatory and inhibitory time-constants,

respectively. Collectively, our findings demonstrate distinct functional consequences of tau and A β at the level of circuits where cellular and molecular changes of AD pathophysiology possibly converge, and provide a rationale to identify potential mechanisms of excitation-inhibition imbalance, hyperexcitability, and abnormal neural synchronization in AD patients that could help guide future clinical studies.

4.1. Abnormal excitatory and inhibitory time-constants represent differential functional consequences of AD pathophysiology at circuit-level

Unlike invasive basic science approaches that can be designed to examine causal relationships, clinical investigations for the most part are limited to examine associative relationships. Nonetheless, the associative links from clinical investigations provide essential building blocks to link the findings from preclinical models to clinical manifestations in patients. NMM is currently by far the most sophisticated tool to investigate circuit function at the level of excitatory and inhibitory neuronal subpopulations in the human brain using non-invasive imaging modalities. The finding that excitatory and inhibitory time-constant abnormalities are uniquely correlated with higher tau and A β , respectively, draws a few key insights in the context of our evolving understanding of AD pathobiology.

The distinctive association of higher tau accumulations to increased excitatory time-constants which indicate aberrant excitatory function within local ensembles of neuronal subpopulations, is consistent with multiple lines of evidence suggesting how tau affects excitatory function of neural circuits. For example, neuropathological studies in human patients with AD detailing the morphology and location of cells that accumulate tau and degenerate, indicate an increased vulnerability of excitatory neurons to tau related pathomechanisms ([Hyman et al., 1984](#); [Braak and Braak, 1991](#)). In basic science studies, mice expressing mutant human tau demonstrate impaired synaptic transmission of glutamate leading to reduced firing of pyramidal neurons ([Hoover et al., 2010](#); [Fu et al., 2017](#); [Fu et al., 2019](#)) while tau reduction in transgenic mice produce an overall decrease in baseline excitatory neuronal activity and modulated the inhibitory neuronal activity leading to reduced network

excitation. The collective insight from these observations indicates a relative vulnerability of excitatory function in neural networks to tau and a resulting network hypoactivity([Harris et al., 2020](#)). Two key findings from the current study are consistent with this discernment, and include: (1) excitatory neuronal parameters uniquely associated with increased tau depositions; (2) reduced oscillatory activity of alpha band associated with higher tau being partially mediated by abnormal excitatory time-constants. Although these findings do not exclude the possibility of tau directly altering firing patterns of inhibitory neurons([Chang et al., 2021](#)), they support the hypothesis that the effects of tau pathophysiology within local networks manifest as excitatory function deficits.

In contrast to intracellular aggregates of tau, accumulation of A β is extracellular ([Braak and Braak, 1991](#);[Nagy et al., 1995](#)). AD basic science models have demonstrated a range of A β associated pathomechanisms that ranges from toxic effects of different A β forms affecting both excitatory and inhibitory synaptic functions ([Meyer-Luehmann et al., 2008](#);[Busche et al., 2012](#);[Busche et al., 2015](#);[Zott et al., 2019](#)). A potential means by which A β leads to network dysfunction in animal models of AD is abnormal hyperactivity in cortical and hippocampal neurons([Palop and Mucke, 2016](#)). Compelling evidence from AD transgenic mice indicate impaired inhibitory synaptic function as a contributory cause for A β related neuronal hyperactivity([Busche et al., 2008](#);[Busche et al., 2012](#);[Verret et al., 2012](#)).

Our findings draw remarkable parallels to these basic science observations by showing unique associations between inhibitory time-constant abnormalities and higher A β tracer uptake. It is important to reiterate that the current findings indicate an overall inhibitory functional deficit at the level of local networks which in turn may be contributed by abnormal inhibitory as well as excitatory deficits at cellular level. Basic science experiments indeed have identified reduced inhibitory interneuron activity as well as aberrant glutamate transmission as potential underlying causes of network hyperactivity in AD transgenic mice ([Busche et al., 2008](#);[Verret et al., 2012](#);[Zott et al., 2019](#)).

Collectively, findings from this clinical imaging investigation, together with comparable basic science evidence, help bridge a crucial gap between circuit level abnormalities and cellular level abnormalities in AD. A key finding from preclinical AD models is that cellular level changes associated with tau and A β produces a combined functional consequence of altered excitatory-

inhibitory imbalance in neural networks([Palop and Mucke, 2016](#);[Harris et al., 2020](#);[Chang et al., 2021](#);[Maestu et al., 2021](#)). Future studies delineating the mechanistic relationships between increased excitatory and inhibitory time-constants and network hyperexcitability are crucial to understand how tau and A β impair excitatory-inhibitory balance in patients with AD.

Although we found significant impairments in both excitatory and inhibitory gain parameters in AD patients, these did not show significant associations with tau and A β . This result maybe explained in part by the relative smaller effect sizes of gain parameters (compared to time-constants). Another possible explanation for this finding may be related to the type of molecular form associated with pathophysiological effects. In both tau and A β , not only that the soluble, molecular forms are important mediators of neurotoxicity but also their effects predominate during the preclinical stages of the disease([Busche, 2019](#);[Zott et al., 2019](#)). However, PET tracer uptake represents mostly the deposited non-soluble forms of protein accumulations. As such it is possible that abnormal neural gains may represent an early effect of soluble neurotoxins, while abnormal time-constants may represent dynamic effects of network changes indicative of progressive pathophysiological events.

Frequency-specific spectral changes may indicate distinct processes leading to network dysfunction in AD

Although a unifying principle governing the physiology of rhythmic oscillations remains obscure, a commonly accepted principle is that oscillations regulate the top-down processing of local neuronal firing and facilitate long-range interactions ([Uhlhaas et al., 2009](#)). Low frequency delta-theta and mid frequency alpha and beta oscillations employ diverse physiological mechanisms determined by different ionic currents ([Wang, 2010](#)) and have distinct functional roles ([Engel et al., 2001](#)). The prominent view in the current literature is that delta-theta oscillations are positive top-down modulators of local neural activity whereas the power of alpha and beta exert an inhibitory modulation of irrelevant neuronal activity thus reducing the neural noise ([Klimesch, 1999](#)). We speculate that higher delta-theta power associated with increased A β therefore may predispose a dysregulated increase of local firing, which is consistent with the proposed hyperexcitability phenomenon described in both preclinical and clinical AD studies([Palop and Mucke, 2010](#);[Vossel et](#)

al., 2016). Our results are also consistent with the phenomena of opposing modulations from tau and A β resulting in a net effect of reduced activity (Harris et al., 2020). For example, alpha and beta oscillations were positively modulated by A β and negatively modulated by tau, albeit a stronger net negative effect with reduced alpha and beta power. Because alpha oscillations are considered as inhibitory gain controllers of local circuits (Klimesch et al., 2007; Lorincz et al., 2009), it is speculative that a net reduction of alpha may yet again be favorable for a hyperexcitable network status. The positive correlation between the characteristic increase of delta-theta and higher levels of A β , and the negative correlation between increased phosphorylated tau, and alpha and beta oscillatory power, in patients with AD, are also consistent with previous experiments that combined MEG/EEG with A β -PET as well with cerebrospinal fluid protein assays (Canuet et al., 2015; Nakamura et al., 2018; Smailovic et al., 2018; Pusil et al., 2019). Collectively, the multimodal neuroimaging in AD patients in the current study demonstrate how positive oscillatory modulators (delta-theta) are associated with A β , while negative oscillatory modulators (alpha) are associated with tau, and offer new perspectives for network stabilizing therapies. Future studies are warranted to further delineate the contributions from excitatory and inhibitory subpopulation functions towards network hyperexcitability and their interplay with oscillatory spectral changes.

4.2. Limitations

Our findings should be considered in the context of the following limitations. First, it is important to point out that any computational model may not perfectly capture the complex dynamics of structure-function coupling of the human brain. Nonetheless, our model had the advantage of using only a few parameters which were interpretable in terms of the underlying biophysics. While the current study was limited to examine the pathophysiological consequences on network properties in AD patients, it is equally important to understand the same phenomena in normal aging. Finally, the current sample size limited the ability to establish a natural history of the excitatory and inhibitory neuronal parameters, which will be the focus of future investigations.

ACKNOWLEDGEMENTS

We would like to thank all the study participants and their families for their generous support to our research. We would also like to acknowledge Avid Radiopharmaceuticals for enabling the use of the 18F-flortaucipir tracer by providing the precursor.

Funding: This study was supported by the National Institutes of Health grants: K08AG058749 (KGR), F32AG050434-01A1 (KGR), K23 AG038357 (KAV), P50 AG023501, P01 AG19724 (BLM), P50-AG023501 (BLM & GDR), R01 AG045611 (GDR); AG034570, AG062542 (WJ); NS100440 (SSN), DC176960 (SSN), DC017091 (SSN), AG062196 (SSN); a grant from John Douglas French Alzheimer's Foundation (KAV); grants from Larry L. Hillblom Foundation: 2015-A-034-FEL and (KGR); 2019-A-013-SUP (KGR); a grant from the Alzheimer's Association: (PCTR-B-13-288476) (KAV), and made possible by Part the CloudTM, (ETAC-09-133596); a grant from Tau Consortium (GDR & WJJ), and a gift from the S. D. Bechtel Jr. Foundation.

Author contributions: KGR, SSN, AR, GDR, BLM and KPR conceptualized and designed the study, interpreted the results, and contributed to manuscript writing. GDR, WJJ, LI, and RLJ contributed to design, analysis, and interpretation of PET data. PV, CC, XX, HL, DM, KK, AS, LI, RLJ, contributed to data analysis, interpretation of results and manuscript writing. HL, DM contributed to data collection.

Competing interests: KGR, SSN, AR, GDR, KPR, WJJ, HL, DM, MLG, PV, XX, CC, KK, LI, RLJ, AS declare no competing interests relevant to this work. BLM has the following disclosures: serves as Medical Director for the John Douglas French Foundation; Scientific Director for the Tau Consortium; Director/Medical Advisory Board of the Larry L. Hillblom Foundation; and Scientific Advisory Board Member for the National Institute for Health Research Cambridge Biomedical Research Centre and its subunit, the Biomedical Research Unit in Dementia, UK. Kiwamu Kudo is affiliated with Ricoh Company, Ltd and has no other competing interests to declare.

Data and materials availability: All data associated with this study are present in the paper or in the Appendix. Anonymized subject data will be shared on request from qualified investigators for the purposes of replicating procedures and results, and for other non-commercial research purposes within the limits of participants' consent. Correspondence and material requests should be addressed to Kamalini.ranasinghe@ucsf.edu

APPENDIX

1. Appendix Figures

- 1.1. **Appendix figure.1:** Observed and predicted power spectra
- 1.2. **Appendix figure.2:** Regional patterns of NMM parameters and tau- and A β -tracer uptake in patients with AD
- 1.3. **Appendix figure.3:** Associations between tau- and A β -tracer uptake and neuronal gain parameters in patients with AD.
- 1.4. **Appendix figure.4:** Associations between spectral power changes and tau- and A β -tracer uptake after correcting for regional atrophy

2. Appendix Tables

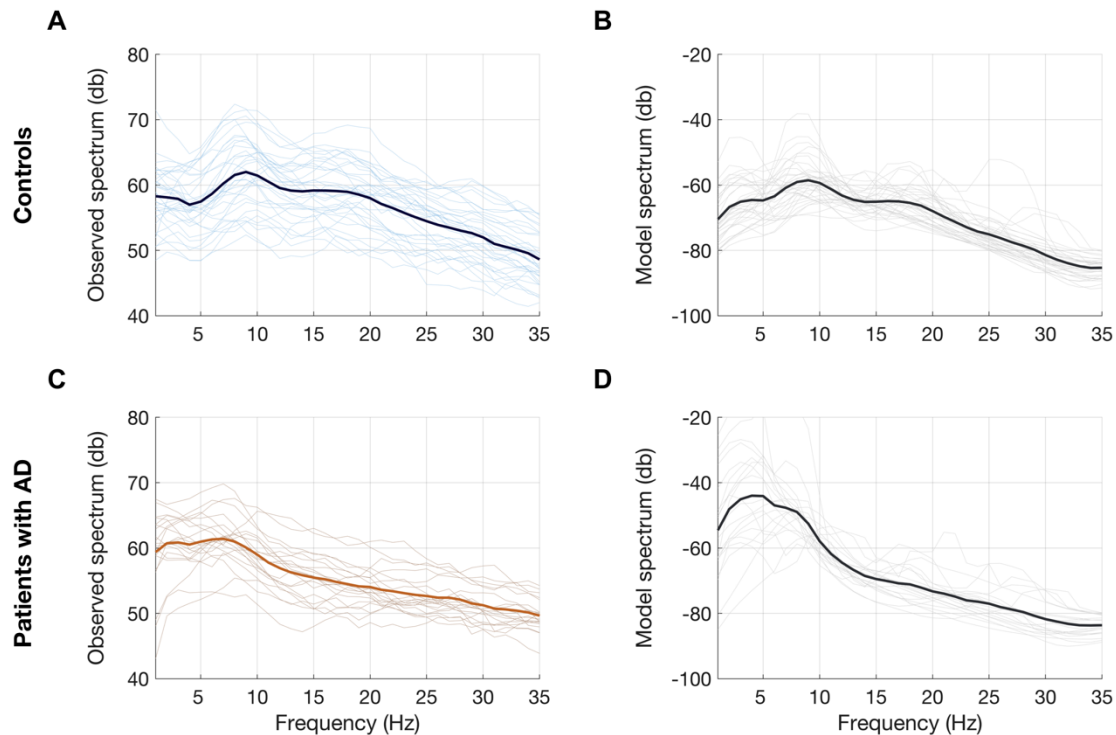
- 2.1. **Appendix table.1:** Neuropsychological test performance in patients with AD

3. Appendix Methods

- 3.1. Resting state MEG data acquisition
- 3.2. Source space reconstruction of MEG data and spectral power estimation
- 3.3. Mathematical modeling and parameter estimation
- 3.4. PET Data acquisition and image processing
- 3.5. Magnetic Resonance image acquisition and analysis

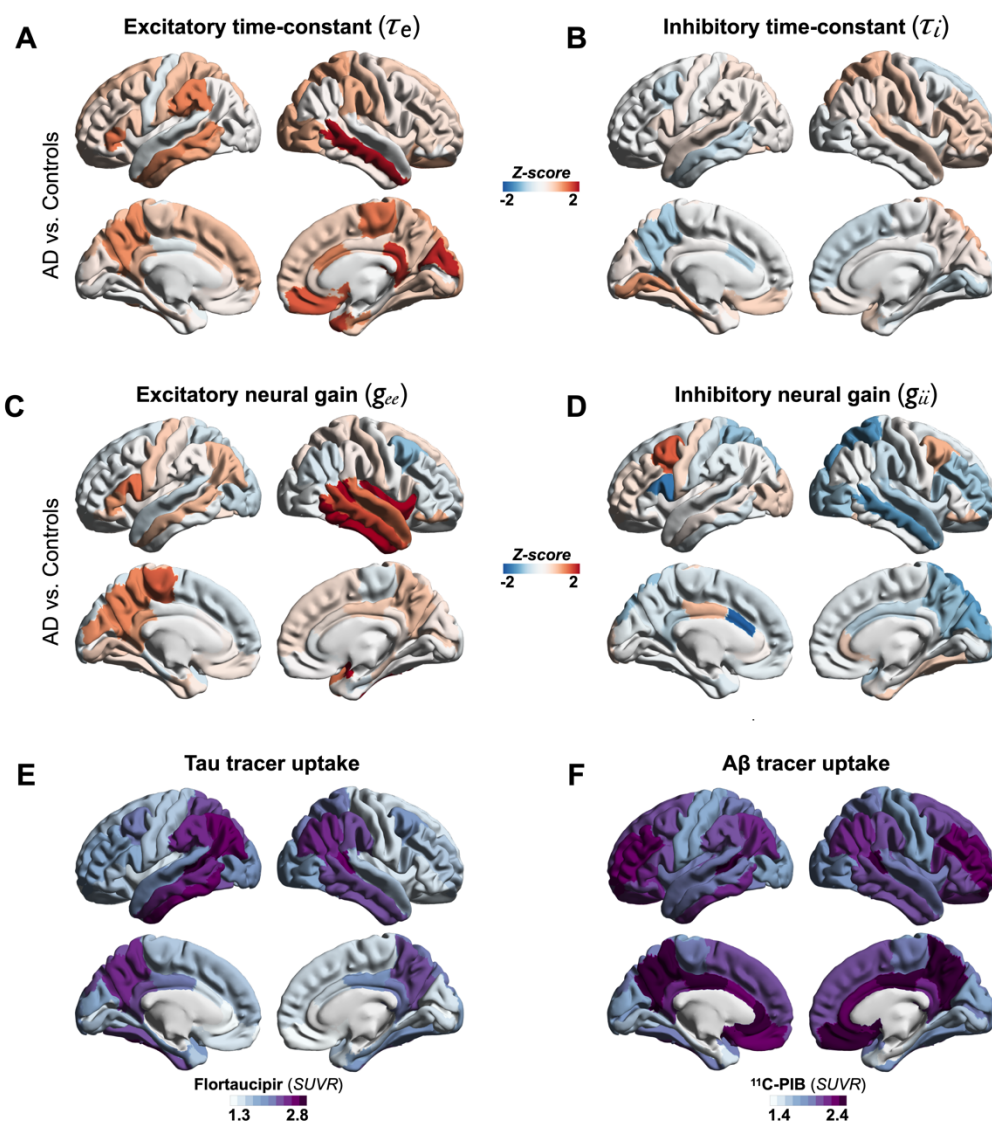
1. Appendix Figures

1.1. Appendix figure.1



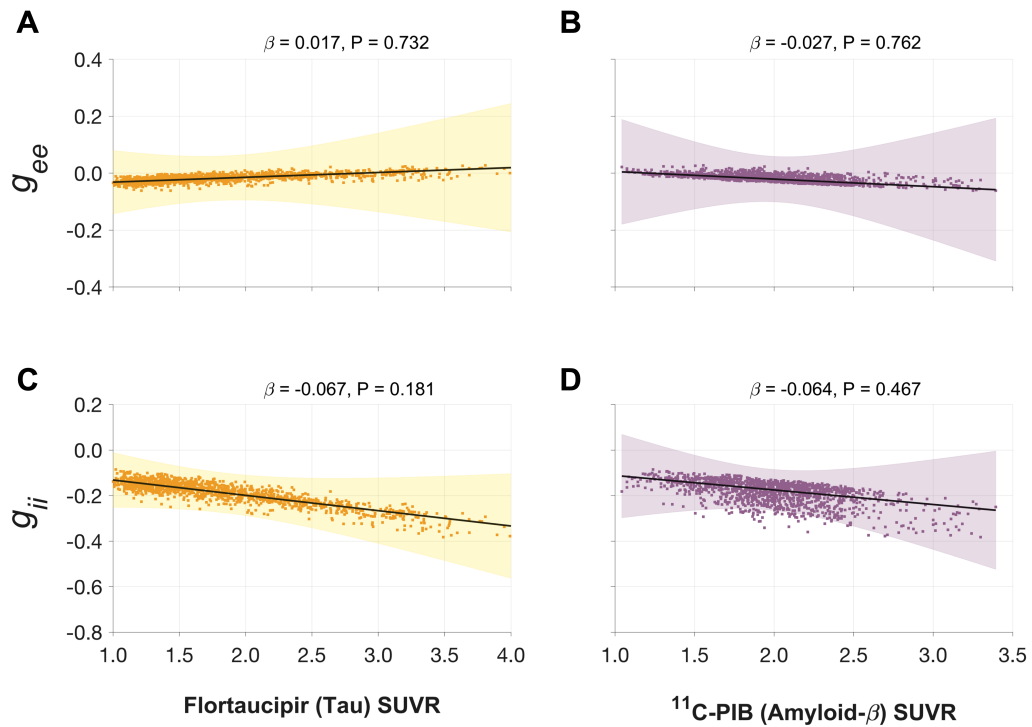
Observed and predicted power spectra in patients with AD and age-matched controls. Observed and model predicted spectra for each participant in the age-matched controls (A-B) and patients with AD (C-D). Each individual line depicts the average spectrum for a given subject across 68 cortical ROIs. The dark line depicts the group averages. The observed spectra are derived from the source space reconstructed MEG time-series data. The model spectra were generated from the linear neural mass model with optimized neuronal parameters for time constants (excitatory, τ_e and inhibitory, τ_i) and neural gains (excitatory, g_{ee} and inhibitory, g_{ii}) to predict the broad-band spectrum (1-35 Hz) optimized to the empirical spectrum derived from MEG. Abbreviations: AD, Alzheimer's disease; MEG, magnetoencephalography; ROI, regions-of-interest.

1.2. Appendix figure.2



Regional patterns of neuronal subpopulation parameters and protein tracer uptakes in patients with AD. Subplots A-D depict the regional differences (z-scores) for excitatory time-constant (A), inhibitory time-constant (B), excitatory gain (C) and inhibitory gain (D) parameters in AD patients with when compared to age-matched controls. Subplots E and F depict the average regional patterns of flortaucipir SUVR (E) and $^{11}\text{C-PIB}$ SUVR (F) for patients with AD showing high flortaucipir retention in temporal lobe, posterior and lateral parietal regions, and high $^{11}\text{C-PIB}$ retention in bilateral frontal and posterior parietal cortices. Abbreviations: AD, Alzheimer's disease; A β , amyloid-beta.

1.3. Appendix figure.3

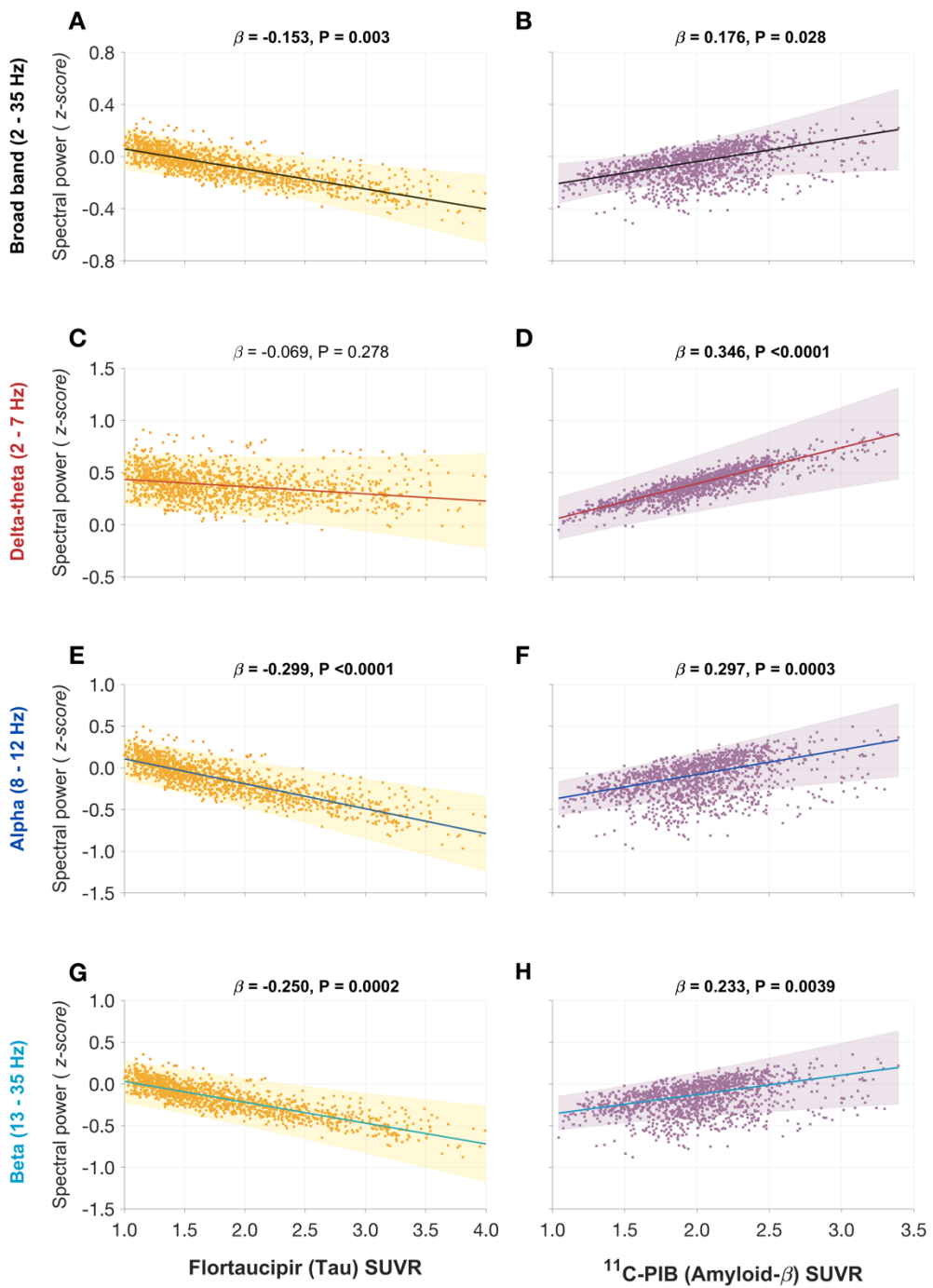


Associations between tau- and A β -tracer uptake and neuronal gain parameters in patients

with AD. Altered gain parameters did not show significant associations with tau and A β in AD patients. Subplots A-D indicate the model estimates from linear mixed effects models predicting the changes (z-scores) in each neuronal parameter from flortaucipir (tau) SUVR and ^{11}C -PIB (A β) SUVR, in patients with AD. The fits depicting tau predictions were computed at the average SUVR of A β (1.99), and the fits depicting A β were computed at average SUVR of tau (1.64). The scatter plots indicate the predicted values from each model incorporating a repeated measures design.

Abbreviations: AD, Alzheimer's disease; A β , amyloid-beta; g_{ee} , excitatory gain; g_{ii} , inhibitory gain; MEG; SUVR, standardized uptake value ratio.

1.4. Appendix figure.4



Associations between spectral power changes and tau- and A β -tracer uptake after correcting for regional atrophy. Tau showed a significant negative association (A), while A β showed a significant positive association (B), with the broad band power spectrum (2-35 Hz). These effects were distinct within

each frequency-specific spectrum. Tau was not associated with the delta-theta (2-7 Hz) spectral changes (C), while it was positively modulated by A β (D). Both alpha (8-12 Hz), and beta (13-35 Hz) spectra showed significant negative associations with tau and significant positive associations with A β (E-H). Each subplot indicates the estimates from linear mixed effects models predicting the spectral power changes from flortaucipir (tau) SUVR and ^{11}C -PIB (A β) SUVR, after including the additional covariate of cortical atrophy in each ROI, in patients with AD. The fits depicting tau predictions were computed at the average SUVR of A β (1.99), while the fits depicting A β were computed at average SUVR of tau (1.64), each at the average w-score of cortical volume (-0.62). The scatter plots indicate the predicted values from each model incorporating a repeated measures design to account for 68 regions per subject. Z-scores for spectral power values were calculated based on the normal control cohort. Abbreviations: AD, Alzheimer's disease; A β , amyloid-beta; SUVR, standardized uptake value

2. Appendix Tables

2.1. Appendix table.1: Neuropsychological test performance in patients with AD

Variable	Test Score (Mean \pm SD)
<u>Episodic memory function</u>	
Visual free recall (Benson 10 minutes)	4.9 \pm 3.2
Short delay verbal memory (CVLT 30 seconds)	3.9 \pm 2.4
Verbal free recall (CVLT 10 minutes)	2.3 \pm 2.9
<u>Executive function & working memory</u>	
Design Fluency	6.4 \pm 2.9
Information processing speed (Stroop color naming)	48.2 \pm 17.6
Cognitive control (Stroop Inhibition)	21.3 \pm 12.9
Verbal working memory (Digit span forward)	5.3 \pm 1.33
Attention (Digit span backward)	3.8 \pm 1.2
Set shifting (Modified trails – speed)	0.2 \pm 0.2
Verbal learning (CVLT total score)	17.9 \pm 6.6
<u>Language function</u>	
Reading irregular words	5.6 \pm 0.7
Syntax comprehension	3.9 \pm 1.2
Verbal Agility	4.6 \pm 1.2
Boston Naming Test	12.3 \pm 3.1
Lexical Fluency (D words/1 minute)	10.8 \pm 5.0
Category Fluency (Animals/1 minute)	11.4 \pm 5.0
Repetition	3.3 \pm 1.4
<u>Visuospatial function</u>	
Face discrimination (CATS – face matching)	10.8 \pm 1.7
Visuoconstruction (Benson copy)	12.8 \pm 4.2
Location discrimination (VOSP number location)	7.5 \pm 2.5
<u>Calculations</u>	3.4 \pm 1.4
<u>Emotion naming</u> (CATS – affect matching)	12.7 \pm 1.0

CVLT=California Verbal Learning Test containing 9 items; CATS=Comprehensive Affect Testing

System; VOSP=Visual Object and Space Perception.

3. Appendix Methods

3.1. Resting state MEG data acquisition

Each subject underwent MEG recording on a whole-head biomagnetometer system consisting of 275 axial gradiometers (MISL, Coquitlam, British Columbia, Canada), for 5-10 minutes. Three fiducial coils including nasion, left and right pre-auricular points were placed to localize the position of head relative to sensor array, and later co-registered to each individual's respective MRI to generate an individualized head shape. Data collection was optimized to minimize within-session head movements and to keep it below 0.5 cm. 5-10 minutes of continuous recording was collected from each subject while lying supine and awake with eyes closed (sampling rate: 600Hz). We selected a 60-second (1 minute) continuous segment with minimal artifacts (minimal excessive scatter at signal amplitude <10 pT), for each subject, for analysis. The study protocol required the participant to be interactive with the investigator and be awake at the beginning of the data collection. Spectral analysis of each MEGI recording and the simultaneously collected scalp EEG recordings were examined to confirm that the 60-second data epoch represented awake, eyes closed resting state for each participant. Artifact detection was confirmed by visual inspection of sensor data and channels with excessive noise within individual subjects were removed prior to analysis.

3.2. Source space reconstruction of MEG data and spectral power estimation

Tomographic reconstructions of the MEG data were generated using a head model based on each participant's structural MRI. Spatiotemporal estimates of neural sources were generated using a time-frequency optimized adaptive spatial filtering technique implemented in the Neurodynamic Utility Toolbox for MEG (NUTMEG; <http://nutmeg.berkeley.edu>). Tomographic volume of source locations (voxels) was computed through an adaptive spatial filter (10 mm lead field) that weights each location relative to the signal of the MEG sensors ([Dalal et al., 2008](#); [Dalal et al., 2011](#)). The source space reconstruction approach provided amplitude estimations at each voxel derived through the linear combination of spatial weighting matrix with the sensor data matrix ([Dalal et al., 2008](#)). A

high-resolution anatomical MRI was obtained for each subject (see below) and was spatially normalized to the Montreal Neurological Institute (MNI) template brain using the SPM software (<http://www.fil.ion.ucl.ac.uk/spm>), with the resulting parameters being applied to each individual subject's source space reconstruction within the NUTMEG pipeline ([Dalal et al., 2011](#)).

To prepare for source localization, all MEG sensor locations were co-registered to each subject's anatomical MRI scans. The lead field (forward model) for each subject was calculated in NUTMEG using a multiple local-spheres head model (three- orientation lead field) and an 8 mm voxel grid which generated more than 5000 dipole sources, all sources were normalized to have a norm of 1. The MEG recordings were projected into source space using a beamformer spatial filter. Source estimates tend to have a bias towards superficial currents and the estimates are more error-prone when we approach subcortical regions, therefore, only the sources belonging to the 68 cortical regions were selected for further analyses. Specifically, all dipole sources were labeled based on the Desikan–Killiany parcellations, then sources within a 10 mm radial distance to the centroid of each brain region were extracted for each region. In this study we examined the broad-band (1-35 Hz) and also the regional power spectra of three frequency bands: 2-7 Hz delta-theta band—a window that captures the full range of low frequency oscillatory activity described in human neurophysiology ([Jacobs, 2014](#); [Goyal et al., 2020](#)), 8-12 Hz alpha band and 13-35 Hz beta band. Power spectra were derived by applying FFT on the time-course data and then converted to dB scale.

3.3. Mathematical modeling and parameter estimation

We used a neural mass model (NMM) ([David and Friston, 2003](#); [Moran et al., 2013](#); [Hartoyo et al., 2020](#)) based on an analytical and linearized version published previously ([Raj et al., 2020](#); [Verma et al., 2022](#)) for estimation of regional model parameters. In this model, for every region k , where k varies from 1 to N and N is the total number of regions based on the Desikan-Killiany parcellation the regional population signal is modeled as the sum of excitatory signals $x_e(t)$ and inhibitory signals $x_i(t)$ (Figure.1D).

Both excitatory and inhibitory signal dynamics consist of a decay of the individual signals with a fixed neural gain, incoming signals from populations that alternate between the excitatory and inhibitory signals, and input Gaussian white noise. The equations for the excitatory and inhibitory signals for every region are the following:

$$\frac{dx_e(t)}{dt} = -\frac{f_e(t)}{\tau_e} * (g_{ee}x_e(t) - g_{ei}f_i(t) * x_i(t)) + p(t) \quad 1$$

$$\frac{dx_i(t)}{dt} = -\frac{f_i(t)}{\tau_i} * (g_{ii}x_i(t) + g_{ei}f_e(t) * x_e(t)) + p(t) \quad 1$$

where $*$ stands for convolution, parameters g_{ee} , g_{ii} , and g_{ei} are neural gains for the excitatory, inhibitory, and alternating populations, respectively, τ_e and τ_i are characteristic time constants of the excitatory and inhibitory populations, respectively, $p(t)$ is the input Gaussian white noise, and $f_e(t)$ and $f_i(t)$ are Gamma-shaped ensemble average neural impulse response functions written as following:

$$f_e(t) = \frac{t}{\tau_e^2} e^{\frac{-t}{\tau_e}} \quad 2$$

$$f_i(t) = \frac{t}{\tau_i^2} e^{\frac{-t}{\tau_i}} \quad 3$$

Since these are linear equations, the closed form solution of $x_e(t)$ and $x_i(t)$ can be obtained in the Fourier domain as $X_e(\omega)$ and $X_i(\omega)$ respectively, where ω is the frequency, by taking a Fourier transform of Equations 1 and 2 as the following:

$$j\omega X_e(\omega) = -\frac{F_e(\omega)}{\tau_e} (g_{ee}X_e(\omega) - g_{ei}F_i(\omega)X_i(\omega)) + P(\omega) \quad 4$$

$$j\omega X_i(\omega) = -\frac{F_i(\omega)}{\tau_i} (g_{ii}X_i(\omega) + g_{ei}F_e(\omega)X_e(\omega)) + P(\omega) \quad 5$$

where j is the imaginary unit, $P(\omega)$ is the Fourier transform of $p(t)$, and $F_e(\omega)$ and $F_i(\omega)$ are written as the following:

$$F_e(\omega) = \frac{\frac{1}{\tau_e^2}}{\left(j\omega + \frac{1}{\tau_e}\right)^2} \quad 6$$

$$F_i(\omega) = \frac{\frac{1}{\tau_i^2}}{\left(j\omega + \frac{1}{\tau_i}\right)^2} \quad 7$$

Solving the above Equations 5 and 6 yields the following:

$$X_e(\omega) = \frac{\left(1 + \frac{\frac{g_{ei}}{\tau_e} F_e(\omega) F_i(\omega)}{j\omega + \frac{g_{ii}}{\tau_i} F_i(\omega)}\right) P(\omega)}{j\omega + \frac{g_{ee}}{\tau_e} F_e(\omega) + \frac{(g_{ei} F_e(\omega) F_i(\omega))^2}{\tau_e \tau_i \left(j\omega + \frac{g_{ii}}{\tau_i} F_i(\omega)\right)}} \quad 8$$

$$X_i(\omega) = \frac{\left(1 - \frac{\frac{g_{ei}}{\tau_i} F_e(\omega) F_i(\omega)}{j\omega + \frac{g_{ee}}{\tau_e} F_e(\omega)}\right) P(\omega)}{j\omega + \frac{g_{ii}}{\tau_i} F_i(\omega) + \frac{(g_{ei} F_e(\omega) F_i(\omega))^2}{\tau_e \tau_i \left(j\omega + \frac{g_{ee}}{\tau_e} F_e(\omega)\right)}} \quad 9$$

Thus, $X_e(\omega)$ and $X_i(\omega)$ can be written as $H_e(\omega)P(\omega)$ and $H_i(\omega)P(\omega)$, respectively, where $H_e(\omega)$ and $H_i(\omega)$ are the transfer functions and $P(\omega)$ is the driving function. The simulated spectra $X(\omega) = X_e(\omega) + X_i(\omega) = (H_e(\omega) + H_i(\omega))P(\omega)$, and the power spectral density is estimated as $\mathbb{E}(|X(\omega)|^2)$, where \mathbb{E} is the expectation. Since the driving function $P(\omega)$ is Gaussian noise which has a flat power spectrum, $\mathbb{E}(|X(\omega)|^2) \propto |H_e(\omega) + H_i(\omega)|^2$. Finally, it is converted to dB scale by calculating $10\log_{10}(|H_e(\omega) + H_i(\omega)|^2)$.

The parameters, g_{ee} , g_{ii} , τ_e , and τ_i were estimated for each region-of-interest (ROI) and parameter g_{ei} was fixed at 1. Each region's spectra were modeled using the above equations, and the power spectral density was generated for frequencies 1-35 Hz. The goodness of fit of the model was estimated by calculating the Pearson's correlation coefficient between the simulated model power

spectra and the empirical source localized MEG spectra for frequencies 1-35 Hz. This goodness of fit value was used to estimate the model parameters. Parameter optimization was done using the basin hopping global optimization algorithm in Python ([Wales and Doye, 1997](#)). The model parameter values and bounds were specified as: 17 ms, 5ms, and 30 ms, respectively, for initial, upper-boundary and lower-boundary, for τ_e , and τ_i ; 0.5, 0.1 and 10, respectively, for initial, upper-boundary and lower-boundary, for g_{ee} and g_{ii} . The hyperparameters of the algorithm which included the number of iterations, temperature, and step-size were set at 2000, 0.1, and 4, respectively. If any of the parameters was hitting the specified bounds, parameter optimization was repeated with a step-size of 6 for that specific ROI, and finally the set of parameters which led to a higher Pearson's correlation coefficient was chosen. The cost function for this optimization was negative of Pearson's correlation coefficient between the source localized MEG spectra in dB scale and the model power spectral density in dB scale as well. This procedure was performed for every ROI of every subject.

In order to examine the effects of model parameters on excitatory and inhibitory activity, $X_e(\omega)/X_i(\omega)$ was calculated while varying each of the parameters g_{ee} , g_{ii} , τ_e , and τ_i one-by-one, keeping others fixed at their estimated mean values calculated for the control cohort. This exploration demonstrated the complex dependency of $X_e(\omega)/X_i(\omega)$ on parameters which varied in a frequency-dependent manner. The complex predictions from g_{ee} and g_{ii} illustrated their control effect on the decay terms in Equations 1 and 2. For instance, when g_{ee} is increased, $x_e(t)$ decays sooner whereas when g_{ii} is increased, $x_i(t)$ decays sooner, leading to a reduction in $x_e(t)$ inhibition and subsequently an increase in $X_e(\omega)/X_i(\omega)$.

3.4. PET Data acquisition and image processing

Detailed descriptions of flortaucipir and PiB PET acquisition are available in previous publications ([Ossenkoppele et al., 2016](#); [Scholl et al., 2016](#)). All PET scans were acquired at Lawrence Berkeley National Laboratory (LBNL) on Siemens Biograph 6 Truepoint PET/CT scanner (Siemens Medical Systems) in 3D acquisition mode. Flortaucipir was synthesized at the LBNL Biomedical Isotope Facility (BIF) using a GE TracerLab FXN-Pro synthesis module with a modified protocol based on an

Avid Radiopharmaceuticals protocol supplied to the facility. Participants were injected with 10 mCi of tracer and scanned in listmode 80-100 minutes post-injection (4x5 min frames). ^{11}C -PIB was also synthesized at the LBNL BIF according to a previously published protocol ([Mathis et al., 2003](#)). Beginning at the start of an injection of 15mCi of PIB into an antecubital vein, 90 min of dynamic emission data were acquired and subsequently binned into 35 frames (4x15s, 8x30s, 9x60s, 2x180s, 10x300s and 2x600s). Flortaucipir and ^{11}C -PIB PET images were reconstructed using an ordered subset expectation maximization algorithm with weighted attenuation and smoothed with a 4 mm Gaussian kernel with scatter correction. Image resolution, calculated using a Hoffman brain phantom, was $6.5 \times 6.5 \times 7.25 \text{ mm}^3$. 90 minutes of dynamic post-injection data for PIB and 80–100 minutes post-injection data for flortaucipir were used for the following PET processing. Each patient's MRI was segmented using Freesurfer 5.3 (<http://surfer.nmr.mgh.harvard.edu>) ([Fischl et al., 2002](#)). PET data were realigned and co-registered onto their corresponding T1 image using the Statistical Parametric Mapping 12 (SPM12, <http://www.fil.ion.ucl.ac.uk/spm/>). Standardized uptake value ratio (SUVR) images were created using Freesurfer-defined cerebellar gray matter for PIB-PET. For FTP, Freesurfer segmentation was combined with the SUIT template ([Diedrichsen, 2006](#)) to only include inferior cerebellum voxels therefore avoiding contamination from off target binding in the dorsal cerebellum ([Baker et al., 2017](#)).

3.5. Magnetic Resonance image acquisition and analysis

Structural brain images were acquired from all participants using a unified MRI protocol on a 3 Tesla Siemens MRI scanner at the Neuroscience Imaging Center (NIC) at UCSF. Structural MRIs were used to generate individualized head models for source space reconstruction of MEG sensor data. The structural MRI scans were also used in the clinical evaluations of patients with AD to identify the pattern of grey matter volume loss to support the diagnosis of AD.

REFERENCES

Albert, M.S., Dekosky, S.T., Dickson, D., Dubois, B., Feldman, H.H., Fox, N.C., Gamst, A., Holtzman, D.M., Jagust, W.J., Petersen, R.C., Snyder, P.J., Carrillo, M.C., Thies, B., and Phelps, C.H. (2011). The diagnosis of mild cognitive impairment due to Alzheimer's disease: recommendations from the National Institute on Aging-Alzheimer's Association workgroups on diagnostic guidelines for Alzheimer's disease. *Alzheimer's & dementia : the journal of the Alzheimer's Association* 7, 270-279.

Babiloni, C., Blinowska, K., Bonanni, L., Cichocki, A., De Haan, W., Del Percio, C., Dubois, B., Escudero, J., Fernandez, A., Frisoni, G., Guntakin, B., Hajos, M., Hampel, H., Ifeachor, E., Kilborn, K., Kumar, S., Johnsen, K., Johannsson, M., Jeong, J., Lebeau, F., Lizio, R., Lopes Da Silva, F., Maestu, F., Mcgeown, W.J., McKeith, I., Moretti, D.V., Nobili, F., Olichney, J., Onofrj, M., Palop, J.J., Rowan, M., Stocchi, F., Struzik, Z.M., Tanila, H., Teipel, S., Taylor, J.P., Weiergraber, M., Yener, G., Young-Pearse, T., Drinkenburg, W.H., and Randall, F. (2020). What electrophysiology tells us about Alzheimer's disease: a window into the synchronization and connectivity of brain neurons. *Neurobiol Aging* 85, 58-73.

Baker, S.L., Maass, A., and Jagust, W.J. (2017). Considerations and code for partial volume correcting [(18)F]-AV-1451 tau PET data. *Data Brief* 15, 648-657.

Bauer, D.J., Preacher, K.J., and Gil, K.M. (2006). Conceptualizing and testing random indirect effects and moderated mediation in multilevel models: new procedures and recommendations. *Psychol Methods* 11, 142-163.

Braak, H., and Braak, E. (1991). Neuropathological stageing of Alzheimer-related changes. *Acta Neuropathol* 82, 239-259.

Busche, M.A. (2019). Tau suppresses neuronal activity in vivo, even before tangles form. *Brain* 142, 843-846.

Busche, M.A., Chen, X., Henning, H.A., Reichwald, J., Staufenbiel, M., Sakmann, B., and Konnerth, A. (2012). Critical role of soluble amyloid-beta for early hippocampal hyperactivity in a mouse model of Alzheimer's disease. *Proc Natl Acad Sci U S A* 109, 8740-8745.

Busche, M.A., Eichhoff, G., Adelsberger, H., Abramowski, D., Wiederhold, K.H., Haass, C., Staufenbiel, M., Konnerth, A., and Garaschuk, O. (2008). Clusters of hyperactive neurons near amyloid plaques in a mouse model of Alzheimer's disease. *Science* 321, 1686-1689.

Busche, M.A., Kekus, M., Adelsberger, H., Noda, T., Forstl, H., Nelken, I., and Konnerth, A. (2015). Rescue of long-range circuit dysfunction in Alzheimer's disease models. *Nat Neurosci* 18, 1623-1630.

Busche, M.A., Wegmann, S., Dujardin, S., Commins, C., Schiantarelli, J., Klickstein, N., Kamath, T.V., Carlson, G.A., Nelken, I., and Hyman, B.T. (2019). Tau impairs neural circuits, dominating amyloid-beta effects, in Alzheimer models in vivo. *Nat Neurosci* 22, 57-64.

Buzsaki, G., Anastassiou, C.A., and Koch, C. (2012). The origin of extracellular fields and currents--EEG, ECoG, LFP and spikes. *Nat Rev Neurosci* 13, 407-420.

Canuet, L., Pusil, S., Lopez, M.E., Bajo, R., Pineda-Pardo, J.A., Cuesta, P., Galvez, G., Gaztelu, J.M., Lourido, D., Garcia-Ribas, G., and Maestu, F. (2015). Network Disruption and Cerebrospinal Fluid Amyloid-Beta and Phospho-Tau Levels in Mild Cognitive Impairment. *J Neurosci* 35, 10325-10330.

Chang, C.W., Evans, M.D., Yu, X., Yu, G.Q., and Mucke, L. (2021). Tau reduction affects excitatory and inhibitory neurons differently, reduces excitation/inhibition ratios, and counteracts network hypersynchrony. *Cell Rep* 37, 109855.

Dalal, S.S., Guggisberg, A.G., Edwards, E., Sekihara, K., Findlay, A.M., Canolty, R.T., Berger, M.S., Knight, R.T., Barbaro, N.M., Kirsch, H.E., and Nagarajan, S.S. (2008). Five-dimensional neuroimaging: localization of the time-frequency dynamics of cortical activity. *NeuroImage* 40, 1686-1700.

Dalal, S.S., Zumer, J.M., Guggisberg, A.G., Trumpis, M., Wong, D.D., Sekihara, K., and Nagarajan, S.S. (2011). MEG/EEG source reconstruction, statistical evaluation, and visualization with NUTMEG. *Computational intelligence and neuroscience* 2011, 758973.

David, O., and Friston, K.J. (2003). A neural mass model for MEG/EEG: coupling and neuronal dynamics. *Neuroimage* 20, 1743-1755.

Diedrichsen, J. (2006). A spatially unbiased atlas template of the human cerebellum. *Neuroimage* 33, 127-138.

Engel, A.K., Fries, P., and Singer, W. (2001). Dynamic predictions: oscillations and synchrony in top-down processing. *Nature reviews. Neuroscience* 2, 704-716.

Fischl, B., Salat, D.H., Busa, E., Albert, M., Dieterich, M., Haselgrove, C., Van Der Kouwe, A., Killiany, R., Kennedy, D., Klaveness, S., Montillo, A., Makris, N., Rosen, B., and Dale, A.M. (2002). Whole brain segmentation: automated labeling of neuroanatomical structures in the human brain. *Neuron* 33, 341-355.

Fu, H., Rodriguez, G.A., Herman, M., Emrani, S., Nahmani, E., Barrett, G., Figueiroa, H.Y., Goldberg, E., Hussaini, S.A., and Duff, K.E. (2017). Tau Pathology Induces Excitatory Neuron Loss, Grid Cell Dysfunction, and Spatial Memory Deficits Reminiscent of Early Alzheimer's Disease. *Neuron* 93, 533-541 e535.

Fu, H.J., Possenti, A., Freer, R., Nakano, Y., Villegas, N.C.H., Tang, M.P., Cauhy, P.V.M., Lassus, B.A., Chen, S., Fowler, S.L., Figueiroa, H.Y., Huey, E.D., Johnson, G.V.W., Vendruscolo, M., and Duff, K.E. (2019). A tau homeostasis signature is linked with the cellular and regional vulnerability of excitatory neurons to tau pathology. *Nature Neuroscience* 22, 47-+.

Goyal, A., Miller, J., Qasim, S.E., Watrous, A.J., Zhang, H.H., Stein, J.M., Inman, C.S., Gross, R.E., Willie, J.T., Lega, B., Lin, J.J., Sharan, A., Wu, C.Y., Sperling, M.R., Sheth, S.A., Mckhann, G.M., Smith, E.H., Schevon, C., and Jacobs, J. (2020). Functionally distinct high and low theta oscillations in the human hippocampus. *Nature Communications* 11.

Harris, S.S., Wolf, F., De Strooper, B., and Busche, M.A. (2020). Tipping the Scales: Peptide-Dependent Dysregulation of Neural Circuit Dynamics in Alzheimer's Disease. *Neuron*.

Hartoyo, A., Cadusch, P.J., Liley, D.T.J., and Hicks, D.G. (2020). Inferring a simple mechanism for alpha-blocking by fitting a neural population model to EEG spectra. *PLoS Comput Biol* 16, e1007662.

Hoover, B.R., Reed, M.N., Su, J., Penrod, R.D., Kotilinek, L.A., Grant, M.K., Pitstick, R., Carlson, G.A., Lanier, L.M., Yuan, L.L., Ashe, K.H., and Liao, D. (2010). Tau mislocalization to dendritic spines mediates synaptic dysfunction independently of neurodegeneration. *Neuron* 68, 1067-1081.

Hyman, B.T., Van Hoesen, G.W., Damasio, A.R., and Barnes, C.L. (1984). Alzheimer's disease: cell-specific pathology isolates the hippocampal formation. *Science* 225, 1168-1170.

Jack, C.R., Jr., Bennett, D.A., Blennow, K., Carrillo, M.C., Dunn, B., Haeberlein, S.B., Holtzman, D.M., Jagust, W., Jessen, F., Karlawish, J., Liu, E., Molinuevo, J.L., Montine, T., Phelps, C., Rankin, K.P., Rowe, C.C., Scheltens, P., Siemers, E., Snyder, H.M., Sperling, R., and Contributors (2018). NIA-AA Research Framework: Toward a biological definition of Alzheimer's disease. *Alzheimers Dement* 14, 535-562.

Jacobs, J. (2014). Hippocampal theta oscillations are slower in humans than in rodents: implications for models of spatial navigation and memory. *Philosophical Transactions of the Royal Society B-Biological Sciences* 369.

Klimesch, W. (1999). EEG alpha and theta oscillations reflect cognitive and memory performance: a review and analysis. *Brain research. Brain research reviews* 29, 169-195.

Klimesch, W., Sauseng, P., and Hanslmayr, S. (2007). EEG alpha oscillations: the inhibition-timing hypothesis. *Brain Res Rev* 53, 63-88.

Lorincz, M.L., Kekesi, K.A., Juhasz, G., Crunelli, V., and Hughes, S.W. (2009). Temporal framing of thalamic relay-mode firing by phasic inhibition during the alpha rhythm. *Neuron* 63, 683-696.

Maestu, F., Cuesta, P., Hasan, O., Fernandez, A., Funke, M., and Schulz, P.E. (2019). The Importance of the Validation of M/EEG With Current Biomarkers in Alzheimer's Disease. *Front Hum Neurosci* 13, 17.

Maestu, F., De Haan, W., Busche, M.A., and Defelipe, J. (2021). Neuronal excitation/inhibition imbalance: core element of a translational perspective on Alzheimer pathophysiology. *Ageing Res Rev* 69, 101372.

Mathis, C.A., Wang, Y., Holt, D.P., Huang, G.F., Debnath, M.L., and Klunk, W.E. (2003). Synthesis and evaluation of 11C-labeled 6-substituted 2-arylbenzothiazoles as amyloid imaging agents. *J Med Chem* 46, 2740-2754.

Mckhann, G.M., Knopman, D.S., Chertkow, H., Hyman, B.T., Jack, C.R., Jr., Kawas, C.H., Klunk, W.E., Koroshetz, W.J., Manly, J.J., Mayeux, R., Mohs, R.C., Morris, J.C., Rossor, M.N., Scheltens, P., Carrillo, M.C., Thies, B., Weintraub, S., and Phelps, C.H. (2011). The diagnosis of dementia due to Alzheimer's disease: recommendations from the National Institute on Aging-Alzheimer's Association workgroups on diagnostic guidelines for Alzheimer's disease. *Alzheimer's & dementia : the journal of the Alzheimer's Association* 7, 263-269.

Meyer-Luehmann, M., Spires-Jones, T.L., Prada, C., Garcia-Alloza, M., De Calignon, A., Rozkalne, A., Koenigsknecht-Talboo, J., Holtzman, D.M., Bacska, B.J., and Hyman, B.T. (2008). Rapid appearance and local toxicity of amyloid-beta plaques in a mouse model of Alzheimer's disease. *Nature* 451, 720-724.

Moran, R., Pinotsis, D.A., and Friston, K. (2013). Neural masses and fields in dynamic causal modeling. *Front Comput Neurosci* 7, 57.

Nagy, Z., Esiri, M.M., Jobst, K.A., Morris, J.H., King, E.M., McDonald, B., Litchfield, S., Smith, A., Barnetson, L., and Smith, A.D. (1995). Relative roles of plaques and tangles in the dementia of Alzheimer's disease: correlations using three sets of neuropathological criteria. *Dementia* 6, 21-31.

Nakamura, A., Cuesta, P., Fernandez, A., Arahata, Y., Iwata, K., Kuratsubo, I., Bundo, M., Hattori, H., Sakurai, T., Fukuda, K., Washimi, Y., Endo, H., Takeda, A., Diers, K., Bajo, R., Maestu, F., Ito, K., and Kato, T. (2018). Electromagnetic signatures of the preclinical and prodromal stages of Alzheimer's disease. *Brain* 141, 1470-1485.

Ossenkoppele, R., Schonhaut, D.R., Scholl, M., Lockhart, S.N., Ayakta, N., Baker, S.L., O'Neil, J.P., Janabi, M., Lazaris, A., Cantwell, A., Vogel, J., Santos, M., Miller, Z.A., Bettcher, B.M., Vossel, K.A., Kramer, J.H., Gorno-Tempini, M.L., Miller, B.L., Jagust, W.J., and Rabinovici, G.D. (2016). Tau PET patterns mirror clinical and neuroanatomical variability in Alzheimer's disease. *Brain* 139, 1551-1567.

Palop, J.J., Chin, J., and Mucke, L. (2006). A network dysfunction perspective on neurodegenerative diseases. *Nature* 443, 768-773.

Palop, J.J., Chin, J., Roberson, E.D., Wang, J., Thwin, M.T., Bien-Ly, N., Yoo, J., Ho, K.O., Yu, G.Q., Kreitzer, A., Finkbeiner, S., Noebels, J.L., and Mucke, L. (2007). Aberrant excitatory neuronal activity and compensatory remodeling of inhibitory hippocampal circuits in mouse models of Alzheimer's disease. *Neuron* 55, 697-711.

Palop, J.J., and Mucke, L. (2010). Amyloid-beta-induced neuronal dysfunction in Alzheimer's disease: from synapses toward neural networks. *Nature neuroscience* 13, 812-818.

Palop, J.J., and Mucke, L. (2016). Network abnormalities and interneuron dysfunction in Alzheimer disease. *Nat Rev Neurosci* 17, 777-792.

Pusil, S., Lopez, M.E., Cuesta, P., Bruna, R., Pereda, E., and Maestu, F. (2019). Hypersynchronization in mild cognitive impairment: the 'X' model. *Brain* 142, 3936-3950.

Raj, A., Cai, C., Xie, X., Palacios, E., Owen, J., Mukherjee, P., and Nagarajan, S. (2020). Spectral graph theory of brain oscillations. *Hum Brain Mapp* 41, 2980-2998.

Ranasinghe, K.G., Cha, J., Iaccarino, L., Hinkley, L.B., Beagle, A.J., Pham, J., Jagust, W.J., Miller, B.L., Rankin, K.P., Rabinovici, G.D., Vossel, K.A., and Nagarajan, S.S. (2020). Neurophysiological signatures in Alzheimer's disease are distinctly associated with TAU, amyloid-beta accumulation, and cognitive decline. *Sci Transl Med* 12.

Ranasinghe, K.G., Hinkley, L.B., Beagle, A.J., Mizuiri, D., Dowling, A.F., Honma, S.M., Finucane, M.M., Scherling, C., Miller, B.L., Nagarajan, S.S., and Vossel, K.A. (2014). Regional functional connectivity predicts distinct cognitive impairments in Alzheimer's disease spectrum. *NeuroImage. Clinical* 5, 385-395.

Ranasinghe, K.G., Petersen, C., Kudo, K., Mizuiri, D., Rankin, K.P., Rabinovici, G.D., Gorno-Tempini, M.L., Seeley, W.W., Spina, S., Miller, B.L., Vossel, K., Grinberg, L.T., and Nagarajan, S.S. (2021). Reduced synchrony in alpha oscillations during life predicts post mortem neurofibrillary tangle density in early-onset and atypical Alzheimer's disease. *Alzheimers Dement*.

Scholl, M., Lockhart, S.N., Schonhaut, D.R., O'neil, J.P., Janabi, M., Ossenkoppele, R., Baker, S.L., Vogel, J.W., Faria, J., Schwimmer, H.D., Rabinovici, G.D., and Jagust, W.J. (2016). PET Imaging of Tau Deposition in the Aging Human Brain. *Neuron* 89, 971-982.

Smailovic, U., Koenig, T., Kareholt, I., Andersson, T., Kramberger, M.G., Winblad, B., and Jelic, V. (2018).

Quantitative EEG power and synchronization correlate with Alzheimer's disease CSF biomarkers.

Neurobiol Aging 63, 88-95.

Sun, X., Meng, X., Zhang, J., Li, Y., Wang, L., Qin, X., Sui, N., and Zhang, Y. (2012). GABA attenuates

amyloid toxicity by downregulating its endocytosis and improves cognitive impairment. *J*

Alzheimers Dis 31, 635-649.

Uhlhaas, P.J., Pipa, G., Lima, B., Melloni, L., Neuenschwander, S., Nikolic, D., and Singer, W. (2009).

Neural synchrony in cortical networks: history, concept and current status. *Frontiers in integrative neuroscience* 3, 17.

Verma, P., Nagarajan, S., and Raj, A. (2022). Spectral graph theory of brain oscillations--Revisited and

improved. *Neuroimage* 249, 118919.

Verret, L., Mann, E.O., Hang, G.B., Barth, A.M., Cobos, I., Ho, K., Devidze, N., Masliah, E., Kreitzer, A.C.,

Mody, I., Mucke, L., and Palop, J.J. (2012). Inhibitory interneuron deficit links altered network activity and cognitive dysfunction in Alzheimer model. *Cell* 149, 708-721.

Vossel, K.A., Ranasinghe, K.G., Beagle, A.J., Mizuiri, D., Honma, S.M., Dowling, A.F., Darwish, S.M.,

Van Berlo, V., Barnes, D.E., Mantle, M., Karydas, A.M., Coppola, G., Roberson, E.D., Miller, B.L.,

Garcia, P.A., Kirsch, H.E., Mucke, L., and Nagarajan, S.S. (2016). Incidence and impact of

subclinical epileptiform activity in Alzheimer's disease. *Ann Neurol* 80, 858-870.

Wales, D.J., and Doye, J.P.K. (1997). Global optimization by basin-hopping and the lowest energy

structures of Lennard-Jones clusters containing up to 110 atoms. *Journal of Physical Chemistry A*

101, 5111-5116.

Wang, X.J. (2010). Neurophysiological and computational principles of cortical rhythms in cognition.

Physiological reviews 90, 1195-1268.

Zhou, L., McInnes, J., Wierda, K., Holt, M., Herrmann, A.G., Jackson, R.J., Wang, Y.C., Swerts, J.,

Beyens, J., Miskiewicz, K., Vilain, S., Dewachter, I., Moechars, D., De Strooper, B., Spires-Jones, T.L., De Wit, J., and Verstreken, P. (2017). Tau association with synaptic vesicles causes

presynaptic dysfunction. *Nat Commun* 8, 15295.

Zott, B., Simon, M.M., Hong, W., Unger, F., Chen-Engerer, H.J., Frosch, M.P., Sakmann, B., Walsh, D.M., and Konnerth, A. (2019). A vicious cycle of beta amyloid-dependent neuronal hyperactivation. *Science* 365, 559-565.

FIGURE LEGENDS

Figure. 1 Spectral power changes and altered excitatory and inhibitory neuronal subpopulations parameters in patients with AD.

Patients with AD showed higher delta-theta (2-7 Hz) spectral power and lacked a clear alpha peak (8-12 Hz) as opposed to controls (A). A two-way-ANOVA comparing patients and controls showed significantly higher spectral power within delta-theta frequency band and showed significantly lower spectral power within alpha and beta (13-35 Hz) bands, in patients with AD (B). The markers depict the least-square means, and the error-bars depict the 95% confidence intervals. Regional patterns of spectral power changes in patients with AD showed increased delta-theta power is predominant in the frontal regions and reduced alpha and beta spectral power is predominant in the temporoparietal and occipital cortices (C). Images show the t-values from statistical comparison of regional data based on DK atlas parcellations and thresholded at FDR 10%. Schematic representation of the linear neural mass model (NMM) and an example model prediction (D). Linear NMM represents the local assemblies of excitatory and inhibitory neurons into lumped linear systems, at each region-of-interest (ROI). External inputs and outputs are gated through both excitatory and inhibitory neurons. The recurrent architecture of the two pools within a local area is captured by the neuronal time-constants, τ_e and τ_i , and neural gain terms, g_{ee} and g_{ii} , indicating the loops created by recurrents within excitatory, inhibitory and cross-populations. At each ROI, the model delivers these parameters as it predicts the broad-band spectrum (1-35 Hz) optimized to the empirical spectrum derived from MEG. Patients with AD showed significantly increased neuronal time-constants, τ_e and τ_i compared to age-matched controls (E). Patients with AD also showed increased excitatory neural gain (g_{ee}) and reduced inhibitory neural gain (g_{ii}) than controls (c). The markers and error-bars depict the least-square means and 95% confidence intervals. Abbreviations: AD, Alzheimer's disease; MEG, magnetoencephalography.

Figure. 2 Associations between tau- and A β -tracer uptake and excitatory and inhibitory neuronal time-constants in patients with AD.

Increased time-constants showed distinct associations with tau and A β in AD patients.

Increased excitatory time-constant (τ_e) was positively correlated with tau, but not with A β (A, B). Increased inhibitory time-constant (τ_i) was positively correlated with A β , but not with tau (C, D). Subplots A-D indicate the model estimates from linear mixed effects models predicting the changes (z-scores) in each neuronal parameter from flortaucipir (tau) SUVR and ^{11}C -PIB (A β) SUVR, in patients with AD. The fits depicting tau predictions were computed at the average SUVR of A β (1.99), and the fits depicting A β were computed at average SUVR of tau (1.64). The scatter plots indicate the predicted values from each model incorporating a repeated measures design. Abbreviations: AD, Alzheimer's disease; A β , amyloid-beta.

Figure. 3 Frequency-specific spectral power modulations of tau and A β are partially mediated via increased excitatory (τ_e) and inhibitory (τ_i) time-constants.

Associations between tau- and A β -tracer uptake and spectral power changes in patients with AD are depicted in subplots A, B, D, E, G, H. Tau was not associated with the delta-theta (2-7 Hz) spectral changes (A), while it was positively modulated by A β (B). Both alpha (8-12 Hz), and beta (13-35 Hz) spectra showed significant negative associations with tau (D, G) and significant positive associations with A β (E, H). Subplots indicate the model estimates from linear mixed effects analyses predicting the spectral power changes from flortaucipir (tau) SUVR and ^{11}C -PIB (A β) SUVR, for patients with AD. The fits depicting tau predictions were computed at the average SUVR of A β (1.99), while the fits depicting A β were computed at average SUVR of tau (1.64). The scatter plots indicate the predicted values from each model incorporating a repeated measures design to account for 68 regions per subject.

Subplots C, F and I depicts mediation models to examine the direct effects of tau and A β , and the effects mediated through excitatory (τ_e) and inhibitory (τ_i) time-constants on different frequency bands. Delta-theta power increases were significantly affected by A β and was partially mediated through the effect of A β on inhibitory (τ_i) time-constant (C). Alpha power reductions were affected by tau and a small, but a significant fraction of this effect was mediated through the effect of tau on excitatory (τ_e) time-constant (F). Beta power reductions were significantly affected by tau, although there was no statistically significant effect mediated through the effect of tau on excitatory (τ_e) time-constant (I). A β effects on alpha and beta spectral changes were only direct effects with not statistically significant effects mediated through altered inhibitory (τ_i) time-constants. Abbreviations: AD, Alzheimer's disease; A β , amyloid-beta; SUVR, standardized uptake value ratio.

Table 1. Participant demographics and clinical characteristics.

Characteristic	Controls (N=35)	Patients with AD (N=20)	P *
Age – yr	69.3.6 ± 8.4	66.3 ± 9.8	0.237
Female sex – no. (%)	20 (57.1)	11 (55.0)	0.876
White – no. (%) [†]	30 (90.9)	20 (100.0)	0.282
Education – yr	18 (16 – 18)	18 (16 – 18)	0.855
Right handedness – no. (%)	30 (85.7)	17 (85.0)	0.340
MMSE [‡]	30 (29 – 30)	23 (22 – 26)	<.0001
CDR [§]	0 (0 – 0)	0.5 (0.5 – 0.8)	<.0001
CDR-SOB [§]	0 (0 – 0)	3.5 (2.3 – 4.3)	<.0001
Age at disease onset	.	59.4 ± 9.39	.
Disease duration	.	6.9 ± 2.4	.

Values for age, age at disease onset and disease duration are means ±SD.

Values for education, Mini Mental State Exam (MMSE), Clinical Dementia Rating (CDR) and CDR-

Sum of Boxes (CDR-SOB), are medians with interquartile ranges within parentheses.

*Statistical tests: P values are reported from unpaired t-test for age, Pearson χ^2 test for sex and handedness, Fisher's exact test for race, Wilcoxon-Mann-Whitney test for education, MMSE, CDR and CDR-SOB.

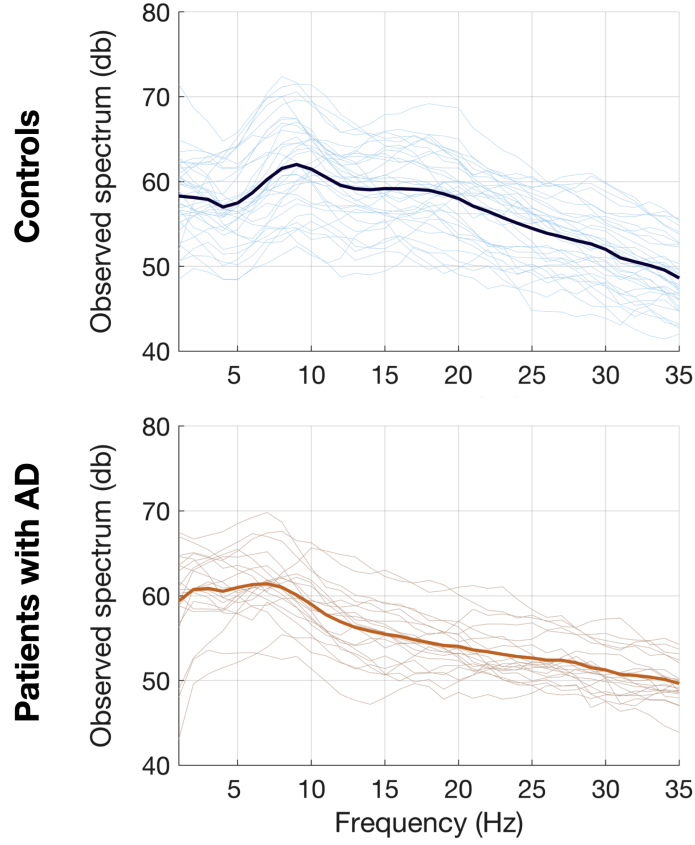
[†]Race or ethnic group was self-reported. Two control participants opted out from reporting the race.

[‡]Scores on the MMSE range from 0 to 30, with higher scores denoting better cognitive function.

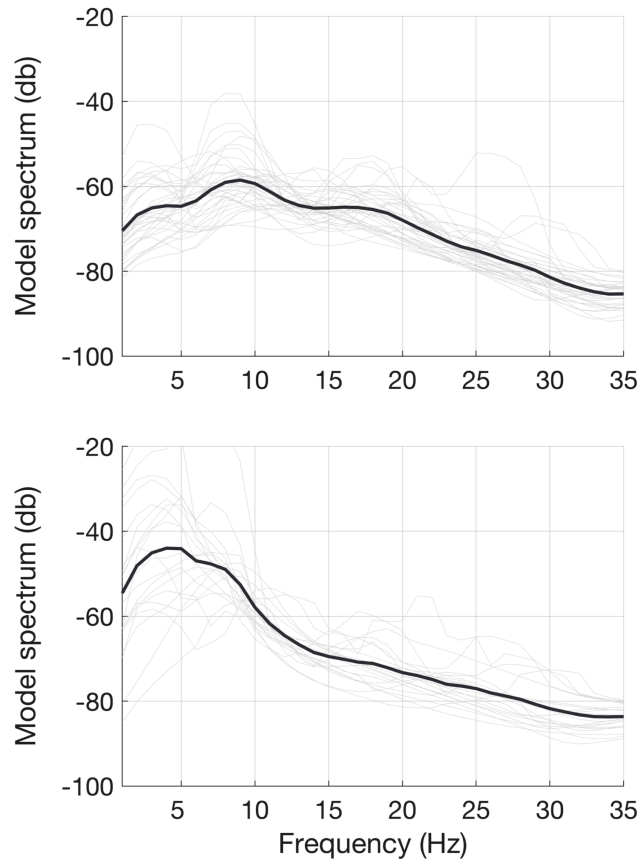
[§]Scores on the CDR range from 0 to 3 and scores on the CDR-SOB range from 0 to 18, with higher scores denoting more disability.

AD = Alzheimer's disease.

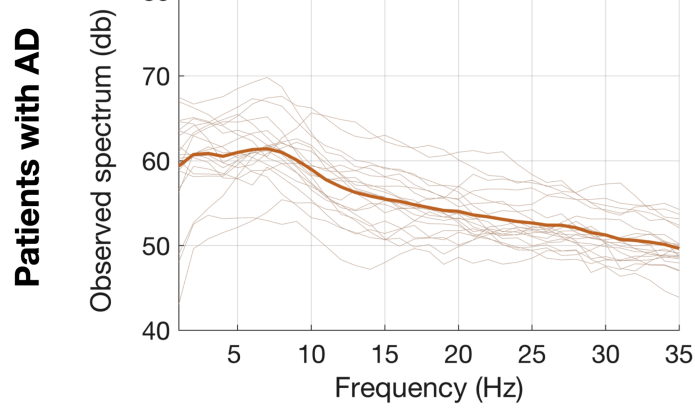
A



B



C



D

